VNIVERSITAT DE VALÈNCIA Facultat de Física

Màster en Física Avançada

Especialitat en Física Teòrica



Treball Fi de Màster

Noisy quantum walks

Andreu Benavent Montell

Tutor: Prof. dr. Armando Perez Cañellas

Co-Tutor: Prof. dr. Andreu Anglés-Castillo

Curs acadèmic 2024/25

Abstract

Quantum walks (QWs) constitute the quantum analogue of classical random walks and have become fundamental tools in quantum computing and quantum simulation. They have become a versatile framework for quantum information processing and for simulating physical phenomena ranging from transport in condensed matter to relativistic dynamics. Their discrete time formulation (DTQWs) exhibits ballistic spreading and rich phenomenology when external fields, nonlinearities, or decoherence are included. We first review the formalism of DTQWs and their continuum limits, which connect the discrete lattice dynamics with the relativistic Dirac equation. We then analyze electric quantum walks (EQWs), where a homogeneous electric field induces distinct transport regimes ranging from ballistic propagation and partial revivals to Anderson localization, depending on the arithmetic properties of the field strength. Subsequently, we study the Nonlinear Optical Galton Board (NLOGB), a nonlinear generalization of the DTQW that supports soliton-like structures by incorporating Kerr-type nonlinearities. The connection with nonlinear Dirac dynamics is highlighted, and conditions for soliton stability are discussed. The central contribution of this work is the incorporation of decoherence through the depolarizing noise channel. By means of numerical simulations, we explore the robustness of EQWs and nonlinear solitons against noise. Our results show that while EQWs gradually lose their distinctive revival and localization features, solitons are particularly fragile, rapidly dispersing under even weak noise. We also analyze long-time behavior through measures such as purity, coherence, and kurtosis, revealing a transition from quantum to diffusive dynamics. These findings provide insight into the interplay of discreteness, nonlinearity, and noise in quantum walks.

Agraiments

Vinc de cor de la Costera,
del poble dels socarrats,
d'allà on renaix de les cendres,
el meu País Valencià.

~ Malaguenya de Barxeta, Obrint Pas amb Pep Gimeno "Botifarra"

Fa cinc anys que vaig entrar per la porta d'aquesta facultat de física, en la que he viscut innombrables històries. Cinc anys després culmine una carrera estudiantil amb aquest treball de fi de màster, que li dona sentit a un cicle i que m'endinsa en una branca de la física en la qual he trobat el meu lloc. És per això que dins d'aquest treball acadèmic, donada la importància personal que té, vull agrair tant a persones com institucions que m'han acompanyat en aquest camí.

Primerament, voldria expressar la meua més sincera gratitud a la Universitat de València, la meua alma mater, en la que he pogut completar la carrera en física i aquest màster. Seguidament, reconéixer la importància de la facultat de física, lloc en el qual se't fa fàcil estudiar una carrera com aquesta. Ací inclouríem a tots els professors que m'han marcat i dels que he aprés. Desgraciadament, no vos puc mencionar a tots, però espere que em recordeu amb l'afecte que jo ho faig. Gràcies per compartir el vostre coneixement i seguir una vida docent. I no m'oblide de l'AdR i de tots els que formeu part, sense vosaltres no havera sigut el mateix.

Ara si, per descomptat, parlar de la meua apreciació més profunda cap a Armando, qui m'ha guiat com a tutor durant aquest procés, i projectes paral·lels. La seua serenitat i paciència, sobretot paciència, han fet que aquest TFM siga possible. Gràcies per obrir-me les portes a la comunitat "quantum computing" de València. En segon lloc, l'estima que tinc cap a Andreu, cotutor d'aquest treball. Allà per tercer de carrera, quan el tenia de professor, m'explicà que era allò de la computació quàntica i va ser tota una revelació en la meua ensenyança. Moltes gràcies per tot el teu suport i coneixement. Et dec alguna cervesa.

No puc oblidar-me tampoc d'Eugeni, qui també ha estat present durant aquest procés i amb qui també he gaudit aprenent un poquet més sobre solitons i òptica quàntica. En la mateixa línia donar-li les gràcies a Carlos, que mai posava cap pega cada vegada que apareixia agobiat pel seu despatx per no entendre alguna cosa.

Naturalment, donar-li també les gràcies a la meua família que sempre m'ha recolzat en aquest procés i m'ha motivat per seguir una carrera acadèmica. En especial a m'abuelo Luis, qui va sembrar la llavor de la ciència en mi. I per acabar, els que mai fallen, gràcies a Nacho, Jaume, Rogante, Marcos i Andreuet per fer d'aquest màster un procés més lleuger, sis cabets pensen més que un. Gràcies a Lola, Pep, Lucía, Fer, David i tots aquells que, pese no saber de física, s'interessaven pel que estudiava i d'alguna forma feien que se'm fera més fàcil l'aprenentatge. Gràcies a tots aquells que heu estat ahí i teniu un lloc en l'aventura.

Contents

1 Introduction **5**
1.1 What is a QW? . . . 5
1.2 This thesis in a nutshell . . . 6

2 DTQW formalism **7**
2.1 Continuum limits in homogeneous DTQWs . . . 9

3 Electric QWs **11**
3.1 Electric QWs formalism . . . 11
3.2 Continuum limit in inhomogeneous DTQWs . . . 11
3.3 Phenomenology of the EQW . . . 12
3.4 Semiclassical Bloch oscillations . . . 14

4 The Non Linear Galton Board (NLOGB) **17**
4.1 The NLOGB through history . . . 17
4.2 NLOGB formalism . . . 18

5 Noisy Quantum Walks **22**
5.1 Noise Model . . . 22
5.2 Numerical implementation . . . 22
5.2.1 Noisy EQWs . . . 23
5.2.2 Noisy Solitons . . . 25
5.3 The noisy NLOGB continuum limit . . . 30

Conclusions **33**

Bibliography **35**

Appendix A: Continued fraction expansion **39**

Appendix B: Lindblad Eq. and PDEs for the NLOGB **40**

Appendix C: Additional material **42**

1 Introduction

1.1 What is a QW?

To first define what a quantum walk (QW) is, we should define its classical analogue. In mathematics, a random walk (also called the Drunkard's walk) is a stochastic process that describes a path consisting of a succession of random steps on some mathematical space. In classical mechanics, we have all studied Brownian motion, which describes the random trajectories of particles suspended in a fluid, where particles occupy well-defined states and the randomness arises from spontaneous transitions between these. But Brownian motion is not the only example; random walks have been extensively used in almost every field of science to model everyday processes such as diffusion and mobility in materials [1], exchange rate forecasts [2], fractal theory [3], and neural synaptic pathways [4]. In this way, random walks form the basis of many algorithms and process theories. It was precisely this algorithmic power that inspired the development of the quantum analogue of the random walk, the so-called quantum walk (QW), firstly introduced by Aharanov et al. [5].

The QW is, in essence, the classical random walk imbued with quantum "magic". To describe it properly, one must invoke three foundational concepts of quantum mechanics: (1) quantum superposition of states, (2) unitary evolution, and (3) collapse of the wave function due to measurement. To visualize this, consider a random walk on a line, that is, a particle moving left or right according to a random coin flip. In the quantum version, one can imagine the particle as a wave packet evolving in superposition. The basic operation in this context is the translation operator, which moves the particle left or right with equal amplitude. However, to truly quantize the translation operation, we need to introduce an additional internal degree of freedom: the spin, which indeed gives rise to superposition. Analogous to a spin-1/2 particle, this internal state can be associated with a two-level system labeled, for instance, as left and right (or up and down). Then, the state of the walker is described by a spinor wave function, and the jump probabilities are conditioned to this internal d.o.f, which plays the role of a quantum coin. The quantum walk proceeds as follows: at each time step, a unitary transformation (a quantum coin) is applied to the spin state of the particle, creating a superposition of left and right. A conditional shift operator then moves the particle to neighboring sites depending on its spin superposition. For example, if a particle is at position 0 in the state $\frac{1}{\sqrt{2}}|\text{right}\rangle + \frac{1}{\sqrt{2}}|\text{left}\rangle$, the evolution operator shifts 50% of the amplitude to position +1 and 50% to position -1. Repeating this process of spin transformation and conditional translation results in a ballistic spread of the probability distribution.

One key distinction between a quantum walk and the propagation of a truly free quantum particle is that the walk takes place on a discrete position space. As a result, its dynamics are not governed by the Schrödinger equation, but instead by unitary maps defined on a lattice. In this thesis, we focus on quantum walks defined in discrete time (DTQWs). However, quantum walks can also be formulated in continuous time (CTQWs), which can be obtained as a limit of DTQWs [6]. Unlike DTQWs, CTQWs are based directly on a Hamiltonian evolution and therefore do not require an additional internal degree of freedom [7]. This makes CTQWs conceptually simpler, and they have been widely implemented in contexts such as quantum transport or search algorithms [8, 9].

Since its theorization [5] it was already pointed out that QWs dispersion is quadratically faster than that of the classical walker. Which means that in the classical case, the probabil-

ity distribution after t steps approaches a Gaussian of variance $\sigma^2 \sim t$. In contrast, quantum walks exhibit a ballistic spreading $\sigma^2 \sim t^2$. This fact kicked off the search for quantum algorithms that performed faster than the classical ones, such as the Groover's algorithm [10]. Then, the most straightforward platform for implementation would be quantum computers. For an implementation proposal of DTQW in quantum circuits see [11], and [12] in complex networks.

However, given that large scale quantum processors are still under development, a variety of alternative experimental platforms have been explored. These include solid state systems, nuclear magnetic resonance setups, optical lattices, and trapped ion architectures [13, 14, 15]. The typical behavior of quantum walks makes it also interesting for the investigation of physical phenomena such as topological phases and protected edge states [16, 17]. And even exotic phenomena have been simulated through QWs such as neutrino oscillations [18], gravitational and gauge fields [19, 20] or extra dimensions in the context of quantum field theory [21].

It is clear that quantum walks play a landmark role in quantum information science, both as algorithmic primitives and for simulating many different quantum scenarios. However, present quantum computers are highly sensitive to classical noise, originating from interactions between qubits and their environment. In this context, we have entered what Preskill coined the *NISQ* era [22], which stands for *Noisy Intermediate Scale Quantum*. Here, *Intermediate Scale* refers to processors ranging from 50 qubits to a few hundreds qubits[1], which is beyond the reach of brute force classical simulation. As Preskill says, "we shouldn't expect NISQ to change the world by itself; instead it should be regarded as a step toward more powerful quantum technologies we'll develop in the future". From this perspective, analyzing the effects of noise on quantum walks becomes a fundamental question in the coming years. For examples of recent work on noisy QW implementations, see [23, 24].

1.2 This thesis in a nutshell

After this introduction, section 2 presents the mathematical formalism of discrete time quantum walks (DTQWs) and their continuum limit. In section 3, the framework is extended to electric quantum walks (EQWs), where the presence of a homogeneous electric field leads to rich phenomenology and analogies with condensed matter phenomena. Section 4 introduces the Nonlinear Optical Galton Board (NLOGB), a nonlinear extension of the DTQW supporting soliton formation. In section 5, we incorporate a noise model through the depolarizing noise channel and study its effect on previously presented models, combining analytical arguments with numerical simulations. The thesis concludes with a synthesis of the main results and our main conclusions.

[1] To this date, IBM posses the largest quantum computer with 1121 qubits.

2 DTQW formalism

To formalize the idea of a quantum walk, consider a simple setup: imagine a particle, i.e., the walker, moving on a one-dimensional discrete lattice. The external degree of freedom, position in the lattice, is labeled by $x = j\epsilon_x$, where $j \in \mathbb{Z}$ is an index labeling the discrete position and ϵ_x is a quantity representing the lattice spacing. The Hilbert space associated with position is denoted by $\mathcal{H}_x$, spanned by the position basis $\{|x\rangle\}_{j\in\mathbb{Z}}$. Then, as mentioned in the introduction, a quantum walk requires an internal degree of freedom: the spin (or coin). This is the quantum analog to the classical bit "0" or "1", which in order to be distinguishable they are imposed to be orthogonal[2]. Thus, the internal d.o.f is described by the coin Hilbert space $\mathcal{H}_c$, spanned by the orthonormal basis $\{|\uparrow\rangle, |\downarrow\rangle\}$. The total Hilbert space of the system is then the tensor product $\mathcal{H} = \mathcal{H}_x \otimes \mathcal{H}_c$, with basis $\{|x\rangle \otimes |\uparrow\rangle, |x\rangle \otimes |\downarrow\rangle\}_{j\in\mathbb{Z}}$, representing a particle at position x with spin either up or down.

Now we ask ourselves: how do the walker move around this lattice? Since the time evolution in quantum mechanics must be unitary, the state of the walker evolves as

$$|\psi(t + \epsilon_t)\rangle = U|\psi(t)\rangle \ , \tag{1}$$

where U is the unitary evolution operator[3], and $\epsilon_t = \epsilon_x = \epsilon$ is the time step[4]. Since this thesis aims to model system-environment interaction, i.e., the initial pure quantum state could evolve to a mixed one, the formalism followed is that of density matrix operators, $\rho(t) = |\psi(t)\rangle\langle\psi(t)|$, so that the unitary evolution becomes

$$\rho(t + \epsilon) = U\rho(t)U^\dagger \ . \tag{2}$$

In close analogy to the classical random walk the unitary evolution U is composite by two unitary operators: S, the shift operator, and C, the coin operator

$$U = SC \ . \tag{3}$$

The coin operator $C = \mathbb{I}_x \otimes R$ acts on the coin space $\mathcal{H}_c$ at each position $|x\rangle$, where $\mathbb{I}_x$ is the identity operator on the position space $\mathcal{H}_x$. The operator R is a rotation of the walker's spin, which mixes the QW components. Written in the coin basis, it belongs to the group $U(2)$ of 2×2 unitary matrices, and can be decomposed into the product of a global phase, $U(1)$, and a special unitary matrix in $SU(2)$ [25]. In particular, the $SU(2)$ matrix can be parametrized using the $SO(3)$ Euler angles, so that the most general form of R is

$$R^{\text{general}} \equiv e^{i\alpha} \begin{pmatrix} e^{i\xi}\cos\theta & e^{-i\zeta}\sin\theta \\ -e^{i\zeta}\sin\theta & e^{-i\xi}\cos\theta \end{pmatrix} \ . \tag{4}$$

However, this general form is unnecessarily redundant if the Euler angles are constant. The global phase α does not affect measurement probabilities, and it can be set to zero. Similarly, the angles ζ and ξ, which generate rotations about the Bloch sphere's z-axis, can be fixed without

[2]Through this work we refer to the internal d.o.f as the spin of a particle, but it could be refereed as two orthogonal states of other system, e.g. the polarization states of a photon or two different atomic energy levels.

[3]For simplicity, the notation omits the hat symbol, $\hat{}$, for operators in capital letters.

[4]This identification simplifies the analysis in the continuum limit. It can also be interpreted as a relativistic condition, implying that the speed unit is $c = 1$. This condition is also known as ballistic scaling.

loss of generality. A common choice is $\zeta = \pi$ and $\xi = 0$, which leads to a standard rotation about the y-axis

$$R = e^{-i\theta\sigma_y} = \begin{pmatrix} \cos\theta & -\sin\theta \\ \sin\theta & \cos\theta \end{pmatrix} , \tag{5}$$

where σ_y is the Pauli matrix acting on the spin states, and θ is the spin mixing angle. In this context, the coin operator C acts locally at each position $|x\rangle$, generating a superposition of $|\uparrow\rangle$ and $|\downarrow\rangle$ states depending on θ's value.

The shift operator, or conditional displacement operator, has the operator representation

$$S \equiv e^{-i\epsilon\hat{p}\sigma_z} , \tag{6}$$

where $\hat{p}$ is the lattice quasi-momentum operator and ϵ, again, the lattice spacing. The Pauli matrix σ_z acts on the coin space, with eigenvalues $+1$ for $|\uparrow\rangle$ and -1 for $|\downarrow\rangle$. The combined action of the operator is thus

$$\begin{aligned} S\,|x,\uparrow\rangle &= |x+\epsilon,\uparrow\rangle \\ S\,|x,\downarrow\rangle &= |x-\epsilon,\downarrow\rangle \end{aligned} . \tag{7}$$

A key feature of the shift operator is that it is entangling. This means it can not be written as the tensorial product of an operator acting on the position space and another acting on the coin space [25].

From now on, we set $x = j$ and $\epsilon = 1$ to simplify the notation; this convention will be reverted later when analyzing the continuum limit. In terms of the basis of $\mathcal{H}$, the shift operator can be written as

$$S = \sum_x |x+1\rangle\langle x| \otimes |\uparrow\rangle\langle\uparrow| \; + \; |x-1\rangle\langle x| \otimes |\downarrow\rangle\langle\downarrow| , \tag{8}$$

which also admits a matrix representation as a block diagonal matrix in the $\mathcal{H}$ space.

With these basic tools, we can already generate the simplest and earliest simulated quantum walk in history [26]. To do so, we set the coin (4) to the so-called Hadamard coin:

$$R_H = \frac{1}{\sqrt{2}} \begin{pmatrix} 1 & 1 \\ 1 & -1 \end{pmatrix} . \tag{9}$$

Then, by setting up a Python simulation (see "Simple Hadamard walk" in the code on [27]), we can run the quantum walk shown in Fig. 1. In this figure, we can already distinguish one of the key differences with its classical analogue: while in the random walk we would expect a final Gaussian probability distribution, here a bimodal distribution is observed at the edges of the walk. This comes from the fact that the walker does not follow a single path, like in the classical walk. It, instead, evolves in a superposition of multiple paths that interfere in a constructive, or destructive, way after each time step.

To wrap up this general formalism, we can express the walker's state in the basis of $\mathcal{H}$ as

$$|\psi(t)\rangle = \sum_x \left[u_{t,x}|x,\uparrow\rangle + d_{t,x}|x,\downarrow\rangle\right] , \tag{10}$$

where the subindex indicate time and space dependence of the up and down components. The

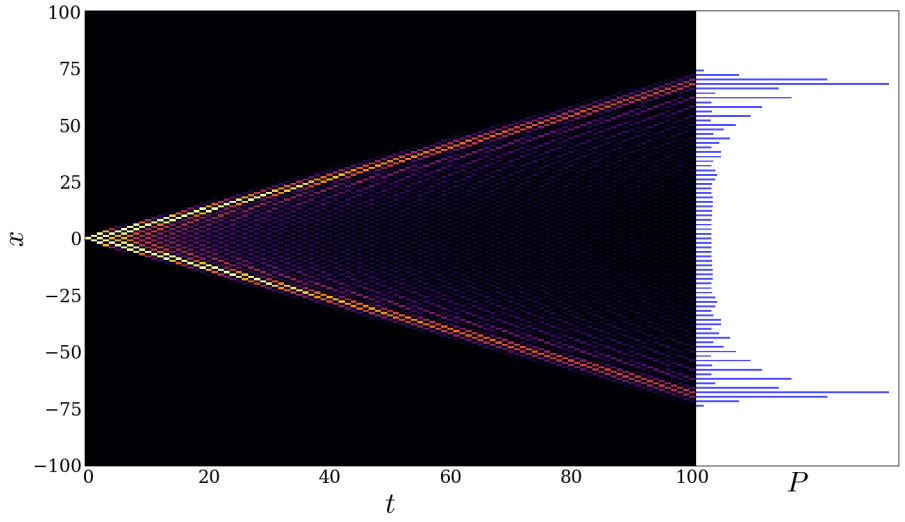


Figure 1: Evolution of the probability density of a localized initial walker at $x = 0$, under a Hadamard coin (9). The initial state is set to be $|\psi(0)\rangle = |0\rangle \otimes \frac{1}{\sqrt{2}}(|\uparrow\rangle + i|\downarrow\rangle)$, resulting in a symmetric bimodal spreading. The QW is performed in a lattice $x \in \{-100, 100\}$ for 100 time steps. Brighter regions correspond to higher probability, and the right side of the picture shows the final, $t = 100$, probability distribution.

corresponding spinor representation is

$$\langle x|\psi(t)\rangle = \Psi(t,x) = u_{t,x}|\uparrow\rangle + d_{t,x}|\downarrow\rangle = \begin{pmatrix} u_{t,x} \\ d_{t,x} \end{pmatrix} . \tag{11}$$

Since this work focuses on open-system effects, we will mainly use the density matrix formalism rather than pure states[5]. The density matrix for a pure state spinor takes the form

$$\rho(t) = |\psi(t)\rangle\langle\psi(t)| = \sum_x \sum_y \left[u_{t,x}|x,\uparrow\rangle + d_{t,x}|x,\downarrow\rangle\right]\left[u^*_{t,y}\langle y,\uparrow| + d^*_{t,y}\langle y,\downarrow|\right] , \tag{12}$$

which projecting onto the position basis yields

$$\langle x|\rho(t)|y\rangle = \langle x|\psi(t)\rangle\langle\psi(t)|y\rangle = \begin{pmatrix} u_{t,x} \\ d_{t,x} \end{pmatrix}\begin{pmatrix} u^*_{t,y} & d^*_{t,y} \end{pmatrix} = \begin{pmatrix} u_{t,x}u^*_{t,y} & u_{t,x}d^*_{t,y} \\ d_{t,x}u^*_{t,y} & d_{t,x}d^*_{t,y} \end{pmatrix} = \begin{pmatrix} \rho^{\uparrow\uparrow}_{x,y} & \rho^{\uparrow\downarrow}_{x,y} \\ \rho^{\downarrow\uparrow}_{x,y} & \rho^{\downarrow\downarrow}_{x,y} \end{pmatrix} . \tag{13}$$

2.1 Continuum limits in homogeneous DTQWs

A QW is referred as an homogeneous DTQW if the coin operator entries in (5) do not depend in space, nor in time. If thats the case, it is well known [6] [25, 19] that the lattice model, Eq.(1), has a continuum limit for $\epsilon \to 0$. Provided that, the richest situation is obtained when the

[5] In [27] this can be seen through the whole code.
[6] What is described here is an intrinsic property of homogeneous DTQWs.

parameters scale with ϵ [19], i.e.,

$$\theta \longrightarrow \epsilon\bar{\theta} \ , \tag{14}$$

and, if the regularity conditions [19] are satisfied. Then we can Taylor expand, in coin basis, the unitary evolution operator using Eq. (5), so that

$$U = e^{-i\epsilon\bar{\theta}\sigma_y}e^{-i\epsilon\hat{p}\sigma_z} \approx (1 - i\epsilon\bar{\theta}\sigma_y + \mathcal{O}(\epsilon^2))(1 - i\epsilon\hat{p}\sigma_z + \mathcal{O}(\epsilon^2)) \approx 1 - i\epsilon\bar{H}(p) + \mathcal{O}(\epsilon^2) \ , \tag{15}$$

with $\bar{H}$ the rescaled Hamiltonian. Introducing this into Eq. (1), it is evident that the unitary evolution tends to the identity (zeroth order) when ϵ tends to 0 and the operator has a valid continuum limit, at first order in ϵ,

$$|\psi(t+\epsilon)\rangle = |\psi(t)\rangle + \epsilon\partial_t|\psi(t)\rangle = \left[\mathbb{I} - i\epsilon\bar{H}(p)\right]|\psi(t)\rangle \longrightarrow i\partial_t|\psi(t)\rangle = \bar{H}|\psi(t)\rangle \ , \tag{16}$$

generated by the rescaled Hamiltonian

$$\bar{H} = \bar{\theta}\sigma_y + \hat{p}\sigma_z \ . \tag{17}$$

This is exactly the 1D Dirac Hamiltonian, in Weyl representation, for a relativistic fermion with mass term $m = \bar{\theta}$. We can also arrive to the 1D Dirac equation by taking Eq. (16) and projecting in the position basis, with Eq. (11),

$$i\partial_t\Psi(t,x) = (\bar{\theta}\sigma_y - i\partial_x\sigma_z)\Psi(t,x) \rightarrow (i\gamma^\mu\partial_\mu - m)\Psi(t,x) = 0 \tag{18}$$

where $\mu = t, x$, $\gamma^t = \sigma_y$ and $\gamma^x = -i\sigma_x$.

Indeed [28], if we remake the reasoning from the more general coin, Eq. (4), the generating Hamiltonian turns out to be

$$\bar{H}^{general} = \sigma_z(\hat{p} + \bar{\xi}) + \mathbf{M}_{\bar{\theta},\bar{\zeta}}\sigma_y - \bar{\alpha}\mathbb{I} \ . \tag{19}$$

Notice that if we input $\bar{\zeta} = \pi$ and $\bar{\alpha} = \bar{\xi} = 0$, then Hamiltonian (17) is recovered. This,(19), is nothing else than the generalization of the 1D Dirac Hamiltonian, for a particle with mass matrix $\mathbf{M}_{\bar{\theta},\bar{\zeta}} = -\bar{\theta}\text{diag}\,(e^{i\bar{\zeta}}, e^{-i\bar{\zeta}})$. Here the fermionic field is coupled to a gauge field with covariant components $A_0 = \bar{\alpha}$ and $A_1 = -\bar{\xi}$. Then, the dynamics of the 1/2-particle, spinor $\langle x|\psi_t\rangle = \psi(x,t)$, are governed by the well known Dirac Equation.

3 Electric QWs

3.1 Electric QWs formalism

During this thesis one of the models analyzed is that of the so called "Electric QW", which has been experimentally implemented [29] and theoretically studied [30]. At heart, adding a homogeneous electric field to the standard DTQW is adding a global phase shift operator that depends linearly on x [30]. This is understood as the operator:

$$E \equiv e^{i\hat{x}\Phi} \; ; \qquad E|x,s\rangle = e^{ix\Phi}|x,s\rangle \; , \tag{20}$$

with s an up or down spin value. Here the constant Φ refers to the electric field and plays a crucial role in the long time propagation properties of the system. Then the full evolution operator is

$$U_\Phi = ECS \tag{21}$$

and the Hamiltonian, in spin basis, generating this evolution

$$H = H_R + H_S + H_E = \theta\,\sigma_y + \hat{p}\,\sigma_z + \Phi\hat{x}\mathbb{I}_c \; , \tag{22}$$

where $\mathbb{I}_c$ is the identity matrix in the coin space $\mathcal{H}_c$. In this case we will allow the coin operator to have complex entries, in general, for $R \in SU(2)$,

$$R = \begin{pmatrix} a & b \\ -\bar{b} & \bar{a} \end{pmatrix} \; , \tag{23}$$

satisfying $|a|, |b| < 1$ and $|a|^2 + |b|^2 = 1$. The reason behind this will be seen later when the *Revival Theorem* is stated [30]. Notice this coin[7], (23), is as general as (4), but without a $U(1)$ global phase. Indeed, this phase comes from the electric field operator (20), in the form of $\alpha = \hat{x}\Phi$. So, essentially, the electric QW is a DTQW with an inhomogeneity in the $U(1)$ phase, which now depends linearly on space.

3.2 Continuum limit in inhomogeneous DTQWs

Previously, in Eq. (19), we found the continuum limit when the parameters of the coin (4) are space-time independent. However, making these space-time dependent still yields the Dirac equation of motion[8] [19], as long as every Euler angle scales equally (through ϵ) to the continuum limit. The PDE obtained in the continuum limit is, following Eq. (18) approach,

$$(i\gamma^\mu D_\mu - m)\psi = 0 \; , \tag{24}$$

where $D_\mu = \partial_\mu - iA_\mu$ is the covariant derivative with $A_0 = \bar{\alpha}(x,t)$ and $A_1 = \bar{\xi}(x,t)$. Notice then, that the mass can be space-time dependent, through the dependence on $\bar{\theta}(x,t)$ shown in (19).

Then, it is evident for the electric QW, Eq. (22), following[9] $E = -\partial_x A_0$, why the corre-

[7] For $a = b = 1/\sqrt{2}$ we recover the usual Hadamard coin, Eq. (9), with a permutation of columns, i.e., a redefinition of up and down components.

[8] Except for the very special case that the zeroth order of θ is an uneven multiple of $\pi/2$, this comes from expanding the general case $\theta(x,t) = \theta_0(x,t) + \epsilon\bar{\theta}(x,t)$.

[9] Remember from electromagnetism that: $\mathbf{E} = -\nabla A_0 - \partial_t \mathbf{A}$.

spondence $\Phi \leftrightarrow E$ is made[10]. Indeed, the general treatment of these angles is extensive and complex and give rise to very interesting phenomenology. It has been seen that through special space-time dependence on the Euler angles the PDE describe the propagation of a Dirac fermion coupled to an electric field, such as the QW studied here, and, possibly, to a general relativistic gravitational field [19, 25, 30].

3.3 Phenomenology of the EQW

This system has already been well studied in the noiseless case by Cedzich et al. [30]. In this paper, Cedzich and colleagues established three types of longtime behavior for the EQW. They realized that small changes in the electric field, Φ or more exactly $\Phi/2\pi$, changed the propagation behavior in the long run. Three distinct regimes arise depending on the arithmetic nature of Φ: the rational, almost rational, and very irrational cases.

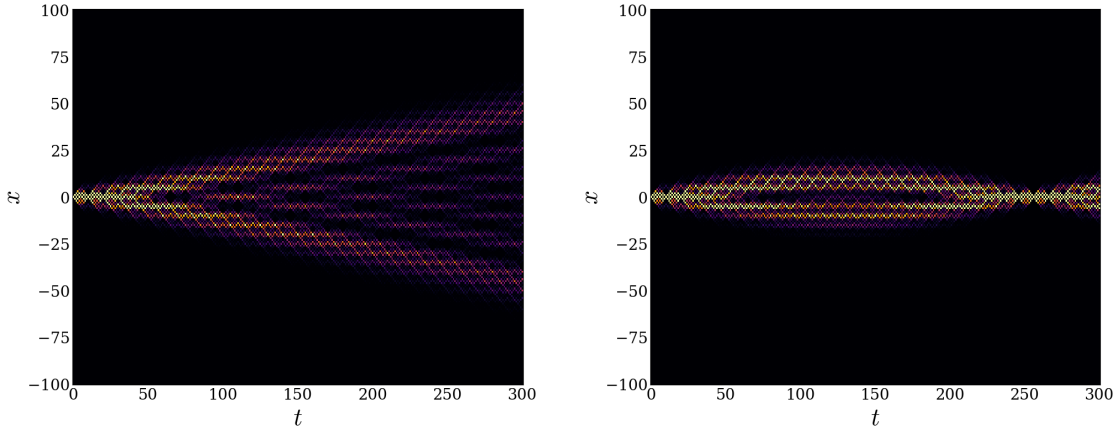


Figure 2: Evolution of the probability density for two EQWs, with electric field values of (a) $\Phi = 2\pi \times 1/5$ and (b) $\Phi = 2\pi \times 51/256$. The coin entries, Eq. (23), are $a = b = 1/\sqrt{2}$. The initial state is $|\psi(0)\rangle = |0\rangle \otimes \frac{1}{\sqrt{2}}(|\uparrow\rangle + i|\downarrow\rangle)$. See "main electric QW" in the code on [27], to see how this plots are created.

In the **rational case**, when $\Phi/2\pi = n/m$ with n and m integers are coprime (no common factors), the walk exhibits quasi-periodic behavior characterized by sharp revivals of the initial state at times $t = m$ or $2m$. This is a consequence of the *Revival Theorem*[11][30], which states:

$$\begin{aligned} \left\| U_\Phi^{2m} + \mathbb{I} \right\|_{\text{op}} &= 2|a|^m \qquad m \text{ odd} \\ \left\| U_\Phi^{m} + (-1)^{m/2}\mathbb{I} \right\|_{\text{op}} &= 2|a|^{m/2} \qquad m \text{ even} \end{aligned} \tag{25}$$

where $||\cdot||_{op}$ stands for operator norm, i.e., the maximum absolute eigenvalue, $\mathbb{I}$ is the identity in the Hilbert space $\mathcal{H}$, and a is one of the input parameters in (23). This theorem state is that after $2m$ steps, for m odd, the unitary evolution is almost the identity up to a global minus sign. Then, the walker's initial state is reproduced after $2m$ steps with accuracy (trace norm distance)

[10] We will refer to Φ as the electric field for convinience.
[11] Proof of which is found in [30].

of $4|a|^m$, which is exponentially small since $|a| < 1$. A similar explanation holds for even m, although there is a small difference coming from the fact that the steps for a state in order to return to the initial state must be even. One of the main outcomes from this theorem is that it yields the dispersion relations for U_Φ^m [30], which determine that the spectrum is continuous, and transport is ultimately ballistic after the revivals end.

In the **almost rational regime**, when $\Phi/2\pi$ is irrational but admits very good rational approximations, meaning that its fraction expansion grows rapidly to large c_i coefficients (see Appendix A), the dynamics are more intricate. The walk exhibits a hierarchy of partial revivals at times given by the denominators m_i of the convergents n_i/m_i to $\Phi/2\pi$ (see Appendix A), with the revival accuracy improving as the next coefficient in the expansion grows. These intermittent revivals are interspersed with extended excursions, during which the walker spreads over large distances before returning to the initial state. This regime gives rise to an interplay between localization and transport, and is characterized by a singular continuous spectrum.

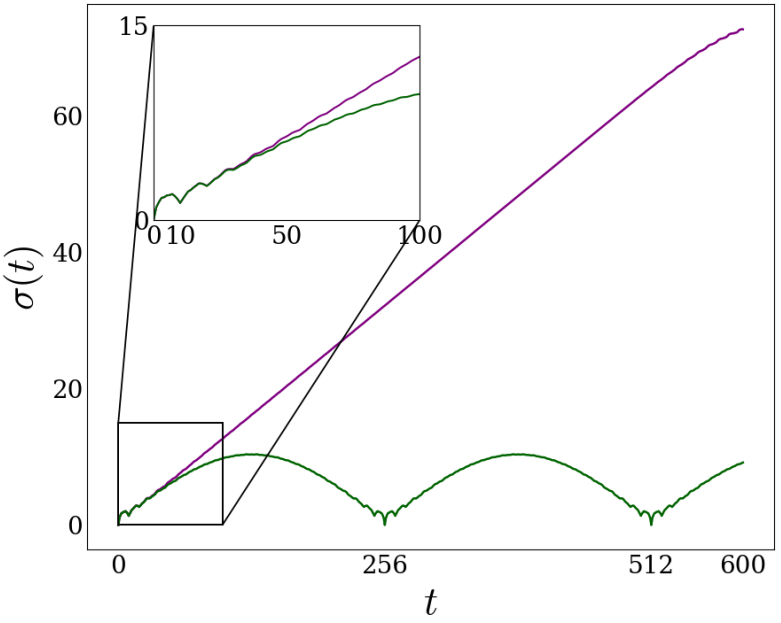
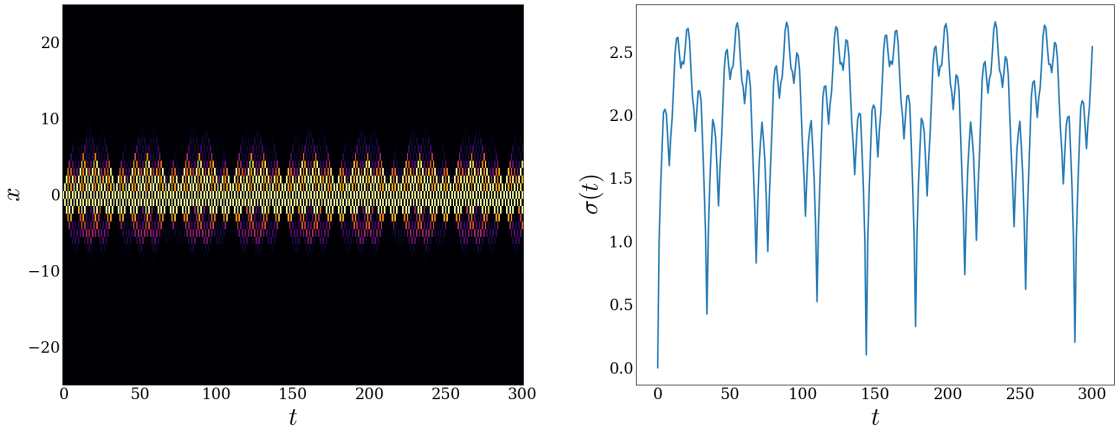


Figure 3: Root mean square, $\sigma(t) = \sqrt{\sum_i x_i^2 P(x_i, t)}$, for both EQWs shown in Fig. 2. Case (a) RMS is followed by the purple curve, whilst case (b) is represented in green.

In Fig. 2 contour plots for two different rational cases are shown. In this, the *Revival Theorem* stated in Eq. (25) is evidenced. In case (a), $m = 5$, which is odd, so the first revival occurs at $t = 10$ (this is even more evident in Fig. 3). Since the error grows exponentially with $m/2$ and $a = 1/\sqrt{2} < 1$, the cumulative error is relatively large, and no second revival is observed. In contrast, for case (b), $m = 256$, a more pronounced revival is observed at $t = 256$. Indeed, because 256 is significantly larger, the error associated with these revivals is much smaller, allowing for additional revivals to be seen in Fig. 3 as zeros of $\sigma(t)$. Furthermore, an interesting behavior can be observed in these figures. The continued fraction expansion of $51/256$ is $(0, 5, 51)$, indicating that $1/5$ is a first-order approximation to $51/256$ (since $1/5 - 51/256 \approx 7.8 \cdot 10^{-4}$). As a result, partial revivals can be seen around integer multiples of 256. This is visible in Fig. 3, reflected

as small sharp peaks around revival times. In this sense, the walk exhibits a hierarchy of partial revivals at times m_i, as previously discussed.

Finally, if $\Phi/2\pi$ is **very irrational**, meaning it is a number with bounded fraction expansion coefficients (see Appendix A), exemplified by the golden ratio[12] $\varphi = (\sqrt{5}-1)/2$ which has $c_i = 1 \ \forall i$, no revivals truly occur, and the wave function becomes exponentially localized around its initial position. This regime is a discrete time analog of Anderson localization: the return probability remains finite, the root-mean-square displacement saturates at a constant value, and the entire spectrum consists of exponentially localized eigenstates forming a pure point spectrum.



(a) (b)

Figure 4: In this plot the probability density evolution for an EQW, with coin (23) entries $a = b = 1/\sqrt{2}$ and electric field value of $\Phi = 2\pi \times (\sqrt{5}-1)/2$ is shown in (a). In (b) the root mean square of the evolution is represented. The initial state is $|\psi(0)\rangle = |0\rangle \otimes \frac{1}{\sqrt{2}}(|\uparrow\rangle + i|\downarrow\rangle)$.

In Fig 4,(a) and (b), the latter case, of very irrational numbers, is illustrated for the golden ratio. There are many peaks, and no tendency for decay or transport is visible. Indeed, the RMS is upper bounded, meaning the return probability to the initial state, $|\langle\psi(0)|\psi(t)\rangle|^2$, never decays to 0. This is the perfect exemplification of Anderson localization in a discrete lattice.

These three regimes illustrate how the arithmetic structure of $\Phi/2\pi$, governs the qualitative nature of quantum transport in electric DTQWs. From perfect revivals and ballistic motion to hierarchical dynamics and Anderson localization, the field parameter acts as a tuner for accessing rich and different phenomenology. However, it is important to emphasize that all of these phenomena rely on the discreteness of the lattice. In the continuum limit, a charged particle in a uniform electric field gets accelerated and no revivals, partial revivals, or localization can occur. Instead, the spectrum becomes unbounded and one recovers the familiar classical motion of uniformally accelerated charged particles.

3.4 Semiclassical Bloch oscillations

In solid state physics, Bloch oscillations refer to the oscillatory motion of a particle, e.g. an electron, subject to a constant electric field while propagating in a lattice described by a tight-

[12] Indeed, its reciprocal. As used in [30].

binding Hamiltonian (TBH). This phenomenon is manifested as an oscillation of the particle's probability distribution with a characteristic period given by $T_{\text{Bloch}}(E) = 2\pi/E$ (for a detailed review, see Refs. [31, 32]). Interestingly, a similar behavior has been observed in DTQWs [33, 34, 35, 30], which corresponds precisely to the scenario described in the previous section, where the period of oscillation is interpreted as the revival time. In both TBHs and DTQWs, when the initial state is localized, the dynamics exhibit a splitting of the initial state into two parts that rejoin after a period of time[13]. However, as we have already discussed, these revivals are not exact in electric QWs, as stated in the *Revival Theorem* (25).

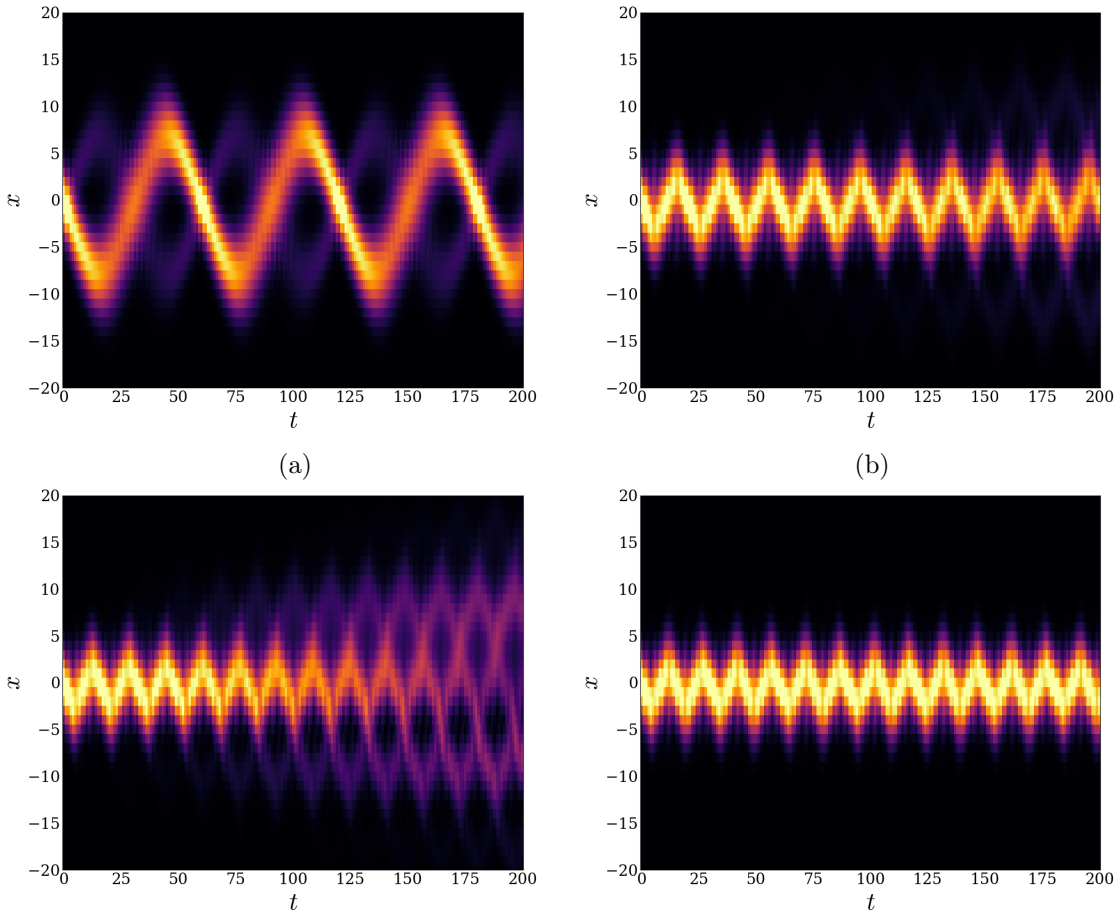


Figure 5: Evolution of the probability density for a walker with an extended initial condition centered in $x = 0$, evolving under a Hadamard coin in the presence of an electric field. The initial state is set to $|\psi(0)\rangle = \sum_x \frac{G(x)}{N}|x\rangle \otimes \frac{1}{\sqrt{2}}(|\uparrow\rangle - |\downarrow\rangle)$, with $G(x)$ a gaussian envelope [Eq. (26)] and N the spatial normalization factor. The values of the electric field used in the simulations are: (a) $\Phi = 2\pi/60$, (b) $\Phi = 2\pi/20$, (c) $\Phi = 2\pi/16$, and (d) $\Phi = 2\pi/15$. The simulations are performed with a $\beta = 0.05$ [see Eq. (26)], following the setup described in [35]. See "Bloch oscillations" in the code on [27], to see how this simulations are performed.

[13]This is referred to as a breathing mode in the context of Bloch oscillations in TBHs.

This description changes when the initial condition is not localized but instead extended. In the case of TBHs, the semiclassical prediction is that a wave packet oscillates about its initial position. But what happens in DTQWs? This question is addressed in [35], where it is shown that for weak electric fields, $2\pi|\Phi| \ll \pi$, and extended initial conditions, the dynamics of electric DTQWs are well approximated by the semiclassical Bloch oscillations of a localized particle evolving under a TBH [31, 32].

The extended initial envelope is chosen to be a Gaussian of the form

$$G(x) = e^{-\beta x^2} \ , \tag{26}$$

which is clearly not normalized. However, since we are performing a numerical analysis this is not a problem if we care to normalize the state initially, since the evolution is unitary. In Fig. 5 these Bloch oscillations can be observed for different values of the electric field. We can see true revivals at times determined by Eq. (25), distinguishing if m, $\Phi/2\pi = n/m$, is odd or even. Notice how the lowest value of the electric field, case (a), corresponds to a fewer number of oscillations. The opposite is also true and can be seen in the other cases, where revivals are not perfect leading to a decrease of the probability density for larger times and richer phenomenology. In (b) this change is tinny, but it is pretty evident in (c). Interesting is the case of (d), where the oscillations are more stable, however it can be seen in Fig. 6 that after more time the standard deviation, σ, evolves linearly with t, turning the propagation ballistic. Interestingly, notice how the slope in σ is so different even for near electric field values of $\frac{1}{15} - \frac{1}{16} \approx 4 \cdot 10^{-3}$!

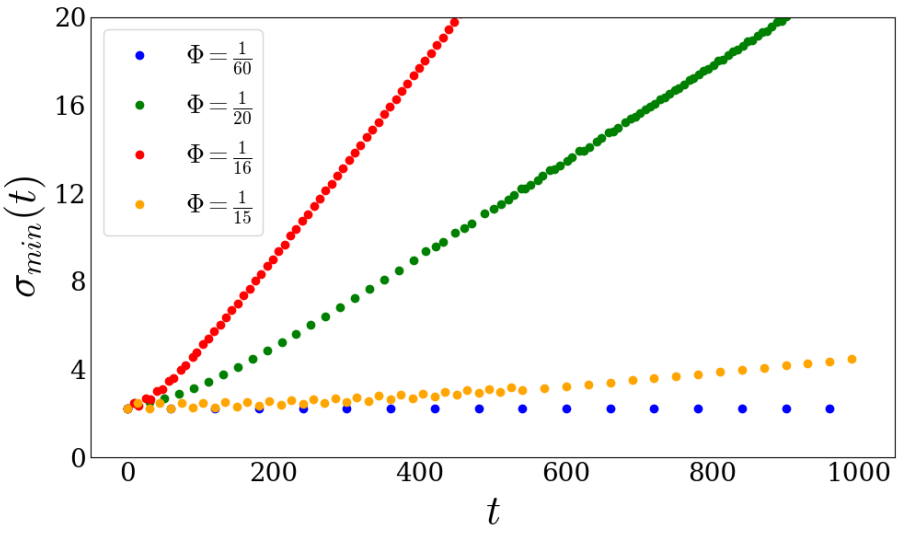


Figure 6: Minima of the standard deviation for the the electric field values presented in Fig. 5, where 2π is erased for clarity in the legend. It could seem that cases such (a) stay oscillating forever, however remember that Eq. 25 taught us that the error is cumulative. At some long t, if $\Phi/2\pi$ is not a bounded irrational, the particle will scape.

4 The Non Linear Galton Board (NLOGB)

4.1 The NLOGB through history

Another QW model treated in this thesis is the Non Linear Optical Galton Board. The Galton board, or quincunx, serves as a physical realization of a classical random walk. It consists of a matrix of regularly spaced pegs through which balls fall under gravity, scattering left or right at each peg. The resulting distribution of balls collected at the bottom follows a binomial distribution. This classical device was revisited by Bouwmeester et al. [36], where Bouwmeester and colleagues introduced the Optical Galton Board (OGB), implemented as a grid of optical Landau–Zener crossings. In their setup, they demonstrated both theoretically and experimentally phenomena such as spectral diffusion and dynamical localization. However, their treatment of light was entirely classical. It wasn't until 2003 [37] that we saw a quantum optical proposal for the Galton board, i.e., an implementation of the quantum walk. Later, in 2005, it was shown by Roldan et al. [38] that the OGB could be reduced to a QW by appropriately tuning the device parameters.

Years later, the work of Navarrete et al. [39] proposed a nonlinear generalization of the Optical Galton Board, known as the *Nonlinear Optical Galton Board* (NLOGB). In this model, nonlinearity is introduced into the evolution of the walker, leading to significant modifications of the standard quantum walk dynamics, now typically referred as nonlinear quantum walk (NLQW). In that work, Navarrete and colleagues ran different simulations identifying three different dynamical ranges for soliton formation.

Solitons are stable, self-reinforcing wave packets that commonly arise as solutions of nonlinear dispersive partial differential equations, where a balance between nonlinearity and dispersion allows them to retain their shape over time. According to Drazin et al. [40], their basic properties include: (1) a permanent form, (2) localization within a finite region, and (3) the ability to interact and emerge from collisions without changing shape. In this sense, Navarrete and colleagues found that soliton formation in the NLOGB is highly sensitive to small variations in the nonlinearity strength, allowing them to distinguish three dynamical regimes. In Fig. 7 it is shown one of such cases, where two soliton structures are created and travel in different directions until both collide and separate indefinitely.

Physically, the added nonlinearity arises from the fact that light propagates not through a linear medium (such as vacuum), but through a nonlinear one, i.e., a Kerr medium, such as in an optical fiber, where the different coin states (u and d) accumulate, independently, a phase after each time step Eq. (29). This nonlinear generalization opens the door to studying rich dynamical phenomena such as soliton formation, self-trapping, and interaction-induced localization, all of which are particularly well-suited to implementation in optical platforms.

In this topic, significant further research has been conducted. Among the extensive bibliography available, we highlight the experimental implementation of the NLOGB reported in [41], which uses the propagation of light pulses in optical fibers. There have also been theoretical studies [42, 43] in which the continuum limit of the NLOGB is identified with a nonlinear Dirac equation. Other works have introduced variations of the NLOGB with three different coin states [44], as well as the inclusion of perturbative potential barriers [45]. We also emphasize the contribution of [46], who present a theoretical and numerical study on the formation, stability, and control of soliton structures in a NLQW. In their model, the nonlinearity is incorporated through

the mixing angle parameter, and one of the main outcomes of this work is the analysis of the continuum limit, which admits solitons as exact stationary solutions.

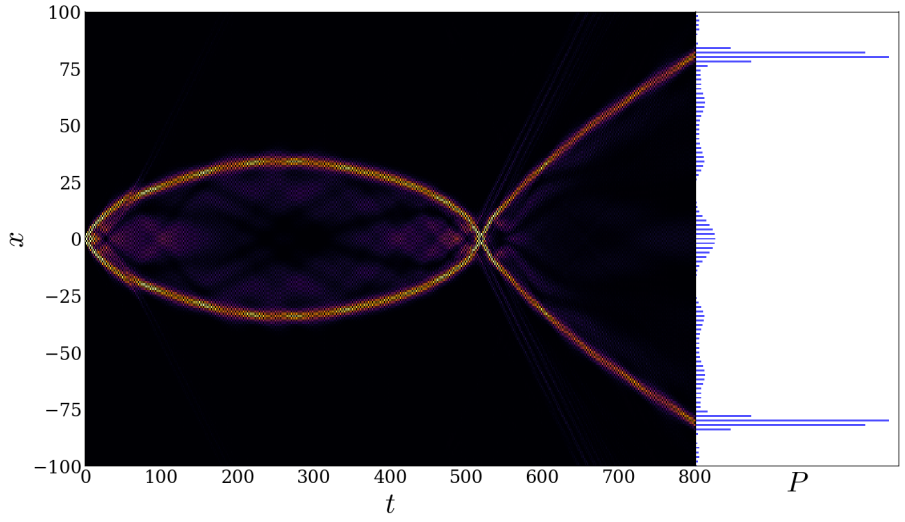


Figure 7: Soliton structure formation, matching Fig. 5 of [39], for $\alpha = 0.49$. The initial state is $|\psi(0)\rangle = |0\rangle \otimes \frac{1}{\sqrt{2}}(|\uparrow\rangle + i|\downarrow\rangle)$, the coin is a Hadamard, (9), and nonlinearity (29) is added to simulate the Kerr medium. The QW is performed in a lattice $x \in \{-200, 200\}$ for 800 time steps.

4.2 NLOGB formalism

Essentially, the NLOGB is a DTQW in which the wavefunction acquires a nonlinear, state-dependent phase depending on the local probability as $\phi_c = i2\pi\alpha|c_{t,x}|^2$, with $c = u, d$, the up and down populations, and α denoting the nonlinearity strength. This nonlinearity can be introduced into the DTQW in various ways. One approach is to replace the standard coin operator with a nonlinear version:

$$R_{t,x} = \begin{pmatrix} e^{i2\pi\alpha|u_{t,x}|^2}\cos\theta & -e^{i2\pi\alpha|d_{t,x}|^2}\sin\theta \\ e^{i2\pi\alpha|u_{t,x}|^2}\sin\theta & e^{i2\pi\alpha|d_{t,x}|^2}\cos\theta \end{pmatrix} . \tag{27}$$

Another method is to introduce the nonlinearity into the shift operator, yielding:

$$S = \sum_x \left[e^{i2\pi\alpha|u_{t,x}|^2}|x+1\rangle\langle x| \otimes |\uparrow\rangle\langle\uparrow| + e^{i2\pi\alpha|d_{t,x}|^2}|x-1\rangle\langle x| \otimes |\downarrow\rangle\langle\downarrow| \right] . \tag{28}$$

However, the approach followed in this work defines a separate nonlinear operator U_{NL}. Which in matrix (coin basis) notation reads:

$$U_{NL} = \begin{pmatrix} e^{i2\pi\alpha|u_{t,x}|^2} & 0 \\ 0 & e^{i2\pi\alpha|d_{t,x}|^2} \end{pmatrix} , \tag{29}$$

clearly diagonal in the basis $\{|x,\uparrow\rangle, |x,\downarrow\rangle\}$. This admits an operator representation by recalling that the spin populations are given by $|u_{t,x}|^2 = \rho_{11}(x,t) = \langle x,\uparrow|\rho|x,\uparrow\rangle$ and $|d_{t,x}|^2 = \rho_{22}(x,t) = \langle x,\downarrow|\rho|x,\downarrow\rangle$, i.e., the diagonal components of Eq. (13), when $x = y$. We then define the

projectors:

$$n_\uparrow(x) = |x,\uparrow\rangle\langle x,\uparrow| = |x\rangle\langle x| \otimes \overbrace{\frac{1}{2}(\mathbb{I}_c + \sigma_z)}^{P_\uparrow} \ , \quad n_\downarrow(x) = |x,\downarrow\rangle\langle x,\downarrow| = |x\rangle\langle x| \otimes \overbrace{\frac{1}{2}(\mathbb{I}_c - \sigma_z)}^{P_\downarrow} \ , \tag{30}$$

where σ_z is the Pauli matrix acting on the coin space and $\mathbb{I}_c$ is the identity matrix on the coin space $\mathcal{H}_c$. With this, the nonlinear part of the Hamiltonian driving the walker evolution can be written as[14]:

$$H_{NL} = -2\pi\alpha \sum_x \left[\rho_{11}(x,t) n_\uparrow(x) + \rho_{22}(x,t) n_\downarrow(x)\right] \ . \tag{31}$$

Hence, the nonlinear evolution operator becomes

$$U_{NL} = e^{-iH_{NL}} \ , \tag{32}$$

which satisfies

$$U_{NL}|x,\uparrow\rangle = e^{i2\pi\alpha|u_{t,x}|^2}|x,\uparrow\rangle \ , \qquad U_{NL}|x,\downarrow\rangle = e^{i2\pi\alpha|d_{t,x}|^2}|x,\downarrow\rangle \ . \tag{33}$$

Overall, the full unitary evolution operator can be written as

$$U = SCU_{NL} \ , \tag{34}$$

where C is the coin operator $(\mathbb{I}_x \otimes R)$, S is the shift (or conditional displacement) operator, and U_{NL} is the nonlinear phase operator.

Moving to the spin basis, the corresponding Hamiltonian generating this unitary evolution is given by

$$H = H_R + H_S + H_{NL} = \theta\,\sigma_y + \hat{p}\,\sigma_z - 2\pi\alpha\left[\rho_{11}(x,t)\,P_\uparrow + \rho_{22}(x,t)\,P_\downarrow\right] \ , \tag{35}$$

where $\theta\,\sigma_y$ generates the coin rotation, $\hat{p}\,\sigma_z$ generates the conditional shift[15], and the last term corresponds to the nonlinear, state-dependent contribution, as previously defined. As a matter of fact, the Hamiltonian above can be interpreted as a discrete analogue of the $1+1D$ Dirac Hamiltonian. In this analogy, the term $\theta\,\sigma_y$ plays the role of a mass term with $m = \theta$, while the kinetic term $\hat{p}\,\sigma_z$ corresponds to the Dirac momentum. The nonlinear contribution acts as a local, state-dependent potential which modifies the evolution according to the local spin value.

In Fig. 8, we represent the evolution of a walker governed by Eq. (34) (see "NLOGB" and specially "NLOGB main code (transitional stage)" in the code on [27]). The initial state is an extended condition borrowed from [46], given by

$$I(x) = \mathrm{sech}(kx), \tag{36}$$

which corresponds to the stationary solution of the continuum equation for an initial state with a relative phase of $-\pi/2$ (which we know support amplification [46]). It is important to note that the model considered in [46] is not equivalent to the one presented here. Therefore, the value of the parameter k is treated as an external input in our case. Nevertheless, the form of

[14] Notice this is in $\mathcal{H}$ basis.
[15] Notice ϵ is already set to 1.

$I(x)$, which is characteristic of solitons [47], remains valid for the NLOGB.

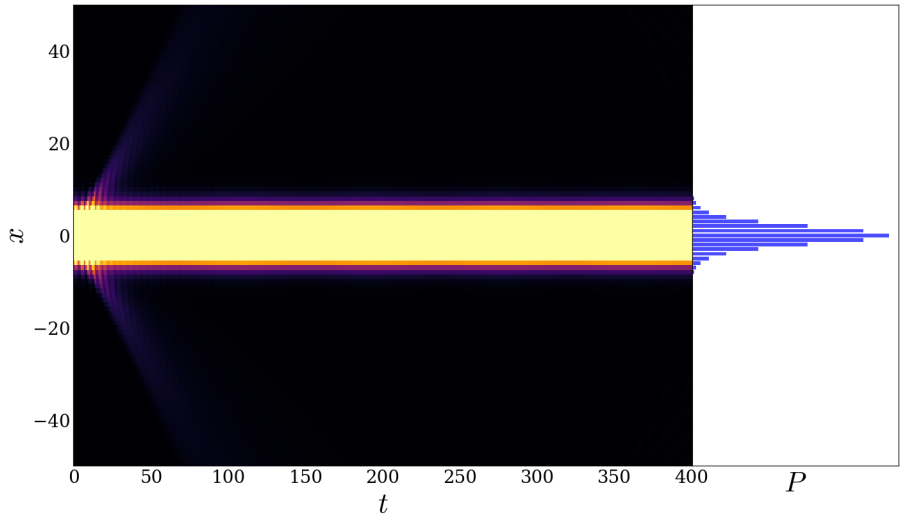


Figure 8: In this figure we plot the evolution of the probability density for an initial extended walker, $|\psi(0)\rangle = \sum_x \frac{I(x)}{N}|x\rangle \otimes \frac{1}{\sqrt{2}}(|\uparrow\rangle + i|\downarrow\rangle)$, under the coin (5) and nonlinear operator (29). N is the spatial normalization factor, and $I(x)$ is determined by Eq. (36). The parameters of the simulation are $\theta = \pi/4$, $\alpha = 0.25$ and $k = 0.4$.

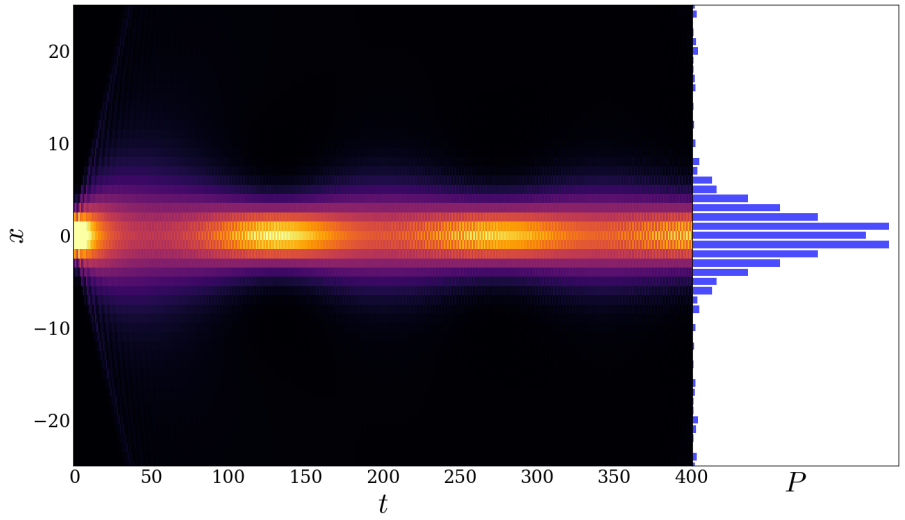


Figure 9: Time evolution of the probability density for an initially extended walker, as in Fig. 8. All parameters are kept fixed, except for the value of k, which now is $k = 0.75$.

Although subtle, Fig. 8 reveals a small probability leakage, approximately 2%, at early times while the remaining $\sim$ 98% of the probability is carried by the soliton. However, as shown in [46], for a given set of parameters θ and α, there exists a specific range of values for k that leads to stable soliton propagation. If k is not properly tuned to match the parameters of the walk,

the resulting state no longer behaves as a soliton. Instead, it exhibits so-called breathing modes, as illustrated in Fig. 9. For comparison, at time $t = 400$, the soliton in Fig. 9 carries only about 75% of the total probability.

5 Noisy Quantum Walks

5.1 Noise Model

The models presented in this work have already been very well studied in the noiseless case [30, 39, 35]. We will go a step further and also incorporate bit-flip and phase-flip decoherence channels, following the approach of [28]. Arnault and colleagues considered that, at each time step $t \to t+1$, the walker undergoes the unitary evolution with probability $1-\pi$, with $\pi \in [0,1]$ a fixed, time-independent probability. This probability is decomposed as $\pi = \pi_x + \pi_z$, where:

- π_x : Is the probability that the system undergoes a bit-flip channel, through unitary σ_x, which flips the coin state: $|\uparrow\rangle \leftrightarrow |\downarrow\rangle$.
- π_z : Is the probability that the system undergoes a phase-flip channel, through unitary σ_z, which transforms $|\downarrow\rangle \to -|\downarrow\rangle$.

These decoherence channels modify the unitary evolution, Eq. (2), following a Lindbaldian form, into[16]:

$$\rho(x,y,t+1) = (1-\pi_x-\pi_z)\,U\rho(x,y,t)U^\dagger + \pi_x\,\sigma_x\rho(x,y,t)\sigma_x + \pi_z\,\sigma_z\rho(x,y,t)\sigma_z\ . \tag{37}$$

where $\rho(x,y,t+1)$ is the density matrix of the walker state[17] at time $t+1$. This form of noise introduces non-unitary decoherence that affects only the internal degree of freedom (spin), leaving the position unchanged. It is, in fact, the so called depolarizing channel [48, 49], without taking into account the σ_y channel (which is a combination of σ_x and σ_z).

Additionally, if the coin used is Hadamard like[18], i.e., following coin (9), then both noise channels, σ_x and σ_z, show a symmetry in the total probability distribution[19] $P(x,t) = \mathrm{Tr}_c[\rho(x,y=x,t)]$. This comes from the fact that both noise channels are unitarily equivalent under the Hadamard transformation, i.e., $\sigma_x = R_H\sigma_z R_H$ and $\sigma_z = R_H\sigma_x R_H$, so it is equivalent applying σ_z to $\rho(x,t)$ and applying σ_x to $R_H\rho(x,t)R_H$. Since the observable $P(x,t)$ is basis independent, then both channels are, in some way, indistinguishable in this special case. For a visual check see the video "Quantum noise channel comparison", on [27], where we represent the cases $\pi = \pi_x = 0.01$ and $\pi = \pi_z = 0.01$. This fact has strong implications in the numerical implementation, so computational power can be saved. The implication of this is extensively used in section 5.2.

5.2 Numerical implementation

In this section we implement the depolarizing channel, Eq. (37), to the models presented in sections 3, EQWs, and 4, NLOGB, with the objective of performing a numerical analysis of how this DTQWs respond to the depolarizing channel. The simulations (see the code on [27]) have been performed in Google Colab, a free, cloud-based environment that allows users to write and

[16] From Eq. (37) notice $\pi_{x,z}$ could seem not to act as probabilities, but instead as coefficients of some other unitary evolution. This is right, since we can understand the evolution of the density matrix as the mean of all the possible paths that the walker could take.

[17] We make explicit the dependence on x and y, since the unitary also affects the position state.

[18] Notice coins (5) and (23) are essentially Hadamard, up to a permutation of rows and columns respectively.

[19] The density matrix is not diagonal on position space, (13), but when probability distribution is considered we have to take the diagonal $y = x$. This is sometimes omitted in the notation for the sake of simplicity.

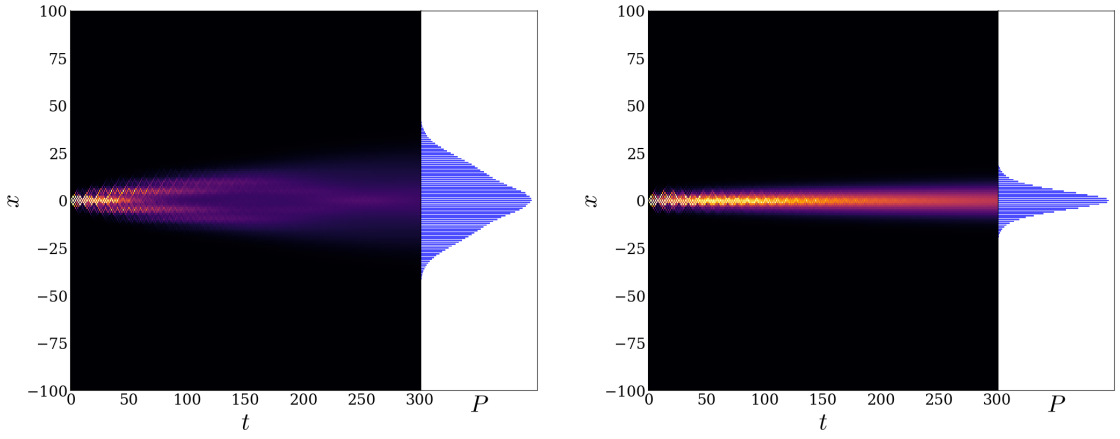
execute Python codes. These Python codes form a large part of the work carried out in this master thesis, so we encourage the lecturer to visit them. The plots already presented were also obtained using these programs, while setting the noise coefficients to 0, i.e., $\pi_x = \pi_z = 0$.

We will skip the standard Hadamard case, Eq. (9) and Fig. 1, since the phenomenology is trivial and already well studied in [28]. The main point of this fundamental case is that the original QW disperses, that is, the probability distribution evolves to a gaussian shape which widens over time. More exactly, as it is pointed out in [28], for the massless case the walker follows the telegrapher equation, Eq. (68) in [28], which solution [50] tends to a gaussian for long times.

This said, we want to numerically check whether the EQWs and NLOGB subject to this depolarizing channel lose their noiseless phenomenology, or if there is any remanent of it.

5.2.1 Noisy EQWs

Firstly, we introduce the depolarizing channel, Eq. (37), in the evolution of the electric quantum walks (EQWs). This is done by choosing the unitary transformation as in Eq. (21) (see "Electric QW" in the code on [27] for how these simulations are implemented).



(a) (b)

Figure 10: Evolution of noisy EQWs for the cases: (a) $\Phi = 2\pi \times 51/256$, corresponding to Fig. 2b, and (b) $\Phi = 2\pi \times (\sqrt{5}-1)/2$, corresponding to Fig. 4. In both cases, the final probability distributions are also shown. The noise parameters are set to $\pi_x = \pi_z = 0.01$, i.e., a total noise strength of 2%.

In Fig. 10 we show two EQWs where the depolarizing channel has been included (see "Electric QW" in the code on [27] for numerical details). The case of a rational electric field is presented in Fig. 10(a), while the irrational case appears in Fig. 10(b). It is clear that the depolarizing channel affects both situations in a similar way: by dispersing the probability distribution. Remarkably, however, the EQW exhibits greater resistance to noise as the electric field becomes more irrational. This is quantified in Fig. 11(a), where a comparison of the spreading deviation for different noise levels[20] is shown for the electric field introduced in section 3.3.

[20] The noise levels are characterized by $\pi = \pi_x + \pi_z$, expressed as a percentage.

Indeed, the phenomenology explained in Sec. 3.3 helps us understand why the different EQWs behave as in Fig. 11(a). According to the *Revival Theorem*, Eq. (25), the error per revival accumulates over time. The depolarizing channel therefore introduces an additional error mechanism that further complicates these revivals. For instance, consider the EQW with $\Phi = \pi(\sqrt{5}-1)$, the golden ratio. As discussed in section 3.3, this case does not accumulate error in the same way, since it does not exhibit true revivals. The depolarizing channel then only adds, depending on the noise level, small errors that translate into diffusion ($\sigma \propto \sqrt{t}$), thereby breaking Anderson localization ($\sigma =$ constant) at long times and leading to the suppression of the oscillations induced by the electric field. In the video "Noisy Golden Ratio EQW comparison" on [27], one can check how these oscillations get suppressed over time for different noise levels, transitioning into a Gaussian shaped curve.

On the other hand, the noiseless rational cases $\Phi = 2\pi \times 51/256$ and $\Phi = 2\pi \times 1/5$ led to ballistic spreading ($\sigma \propto t$), as shown in Fig. 3. Once more, the depolarizing channel modifies these EQWs into a diffusive regime, even converging at high noise strengths (around 10%). Interestingly, the oscillations induced by the electric field remain observable at relatively low noise levels, see Fig. 11(b), although this effect is restricted to early times (less accumulated error). This can also be checked in the videos "Noisy 1 5 EQW comparison" and "Noisy 51 256 EQW comparison" on [27], where, as in the golden ratio case, the oscillations get suppressed, leading to a Gaussian envelope[21].

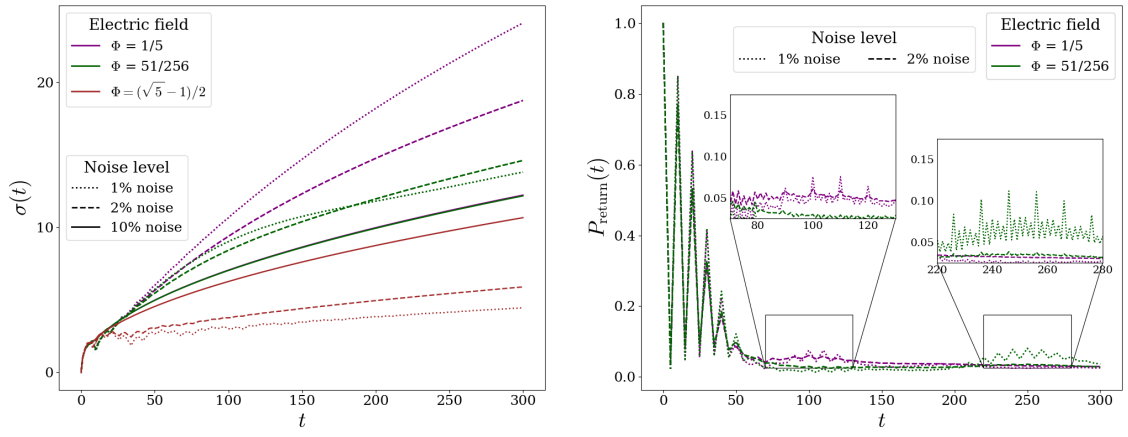


Figure 11: On the left hand side, (a), comparison of the standard deviation, $\sigma(t) = \sum_x x^2 P(x,t)$, for electric fields $\Phi = 1/5$ (purple), $\Phi = 51/256$ (green), and $\Phi = (\sqrt{5}-1)/2$ (red). Noise levels $\pi = \pi_x + \pi_z$ are indicated as follows: 1% (dotted line), 2% (dashed line), and 10% (solid line). On the right hand side, (b), probability of return to the initial state, $|\langle\psi(0)|\psi(t)\rangle|^2$, where $|\psi(0)\rangle = |0\rangle \otimes \frac{1}{\sqrt{2}}(|\uparrow\rangle + i|\downarrow\rangle)$. The return probability is shown for $\Phi = 1/5$ and $\Phi = 51/256$ with the same style as in (a). Note that the factor 2π is omitted for convenience.

Once the phenomenology with localized initial states has been discussed, we can extend the analysis to extended initial conditions, corresponding to the semiclassical Bloch oscillations introduced in section 3.4. The qualitative behavior does not differ significantly: the oscillations

[21] The Gaussianization mentioned is visible in Fig. 20 on Appendix C.

fade progressively over time, as illustrated in Fig. 12. On the right-hand side of Fig. 12, the final probability density can be seen to gradually approach a Gaussian profile, whilst showing small oscillations, due to the electric field. This effect can also be observed in the video "Noisy BO 1 60" on [27].

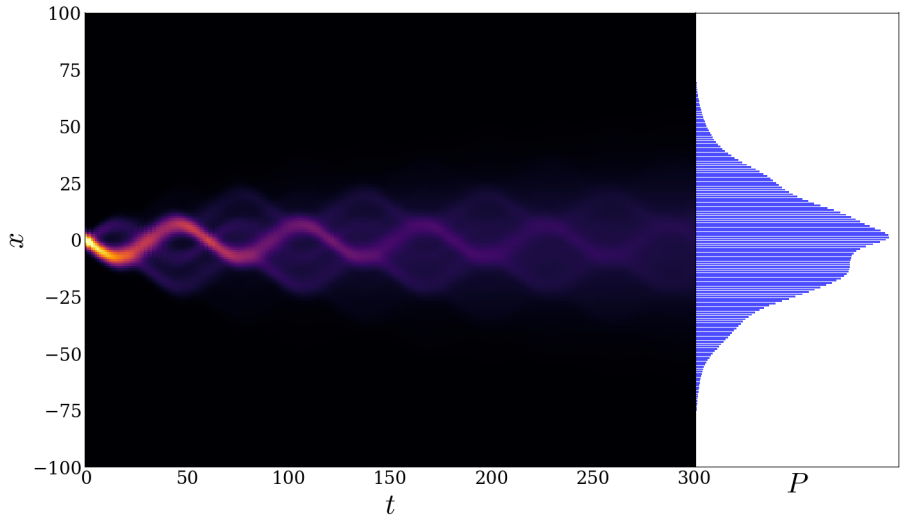


Figure 12: Noisy Bloch oscillations for $\Phi = 2\pi/60$, following the setup of Fig. 5(a). The noise level is set to 2%.

5.2.2 Noisy Solitons

Now, we continue with the application of the depolarizing channel, Eq. (37), in the evolution of the solitons (NLQWs). In this occasion, the unitary transformation is chosen as in Eq. (34), and noise levels, as used before, refer to $\pi = \pi_x + \pi_z$ in percentage.

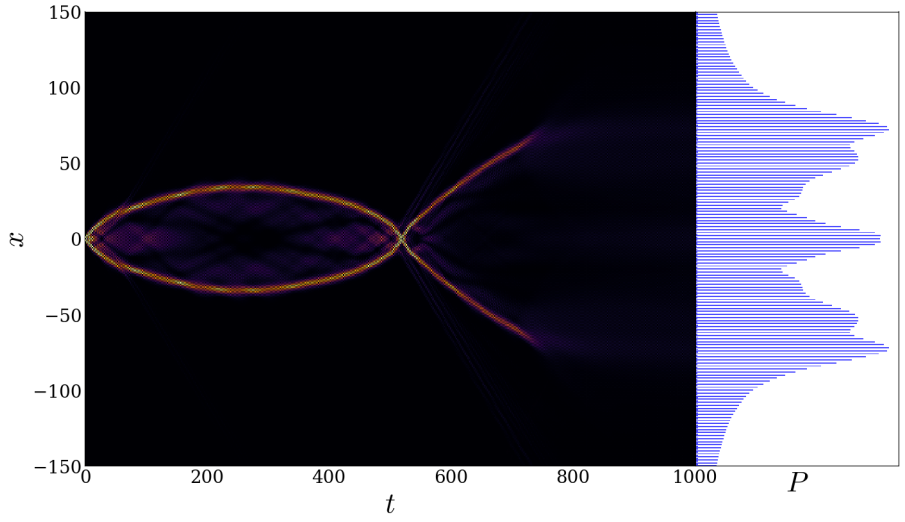


Figure 13: Noisy evolution of the case illustrated in Fig. 7, in the presence of a 1% noise level.

As an illustrative check, we first consider localized initial conditions, i.e., Fig. 7. However, since this is not the main focus of this section, we only examine what happens when the noise channel is activated at a specific time. In this case, since we expected some diffusion, the depolarizing channel is switched on at $t = 700$, when the two soliton wave packets are already completely separated after the collision. This can be seen in Fig. 13, where the diffusion of both solitons is visible on the right-hand side of the figure. A remarkable feature of this case is how the diffusive solitons interfere, not only with each other but also with the internal wave packets, creating a three-peaked distribution that gradually smoothens over time, as shown in the video "Noisy Sauron Eye" on [27].

In line with this approach to noise application in the case of soliton formation with NLQWs, we now turn to the richer case shown in Fig. 8, where extended initial conditions are used. In this scenario, a richer phenomenology was observed in the simulations, leading to a deeper analysis and the collection of more data.

In Fig. 14, three different evolutions of the soliton central regions[22], corresponding to noise values of 0.5%, 20%, and 50%, are presented. From this figure, one can interestingly extract an unexpected result: lower noise levels led to faster dispersion.

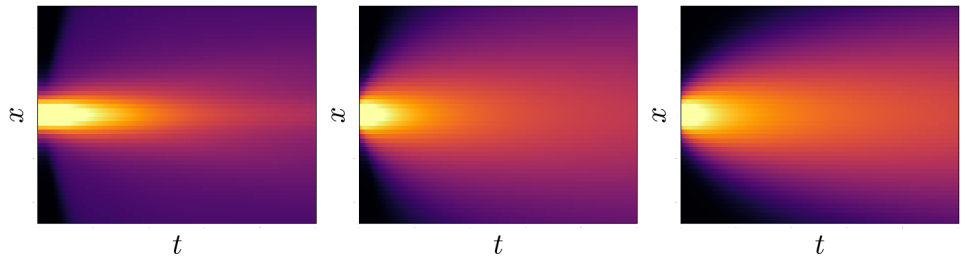
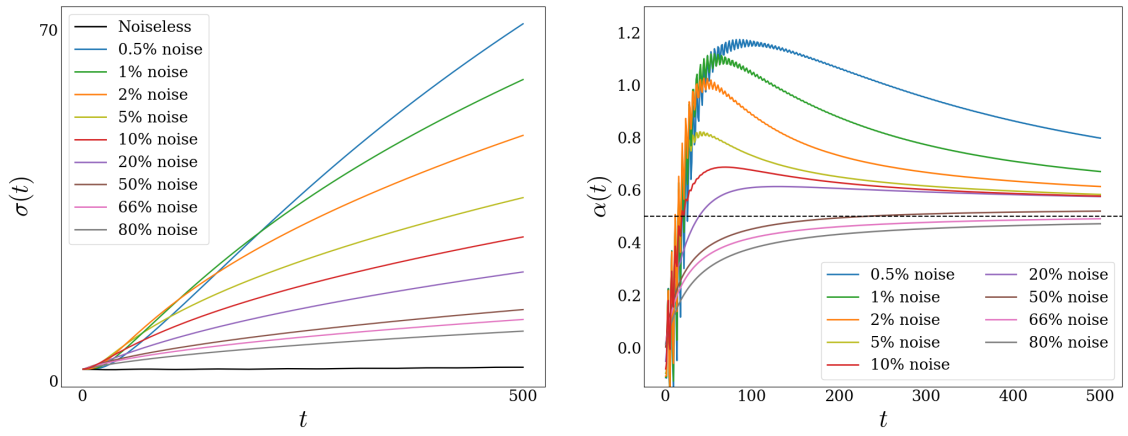


Figure 14: Three different evolutions of the soliton in Fig. 8, simulated on a larger lattice with $x \in [-500, 500]$ and $t_{\text{final}} = 500$. For clarity, only the central region $x \in [-25, 25]$ is shown, with respective noise levels of 0.5%, 20%, and 50%.

This behavior led us to collect more data for different noise levels and to perform several statistical analyses. One of them consists in visualizing the temporal evolution of the standard deviation, so that we can infer how the noise level relates to dispersion. This is shown in Fig. 15 (a), where the standard deviation of nine different noisy solitons is plotted. Interestingly, lower noise levels correspond to faster dispersion of the walker, and vice versa.

This behavior, shown in Fig. 15, highlights the drastic change from the noiseless case to the noisy case, suggesting that the soliton is destroyed almost instantly once the depolarizing channel is applied. This interpretation is consistent with the soliton formation mechanism. As mentioned in previous sections, the relative phase required for soliton formation is $\delta = -\pi/2$ [46]. Now consider the case of individual trajectories. If σ_x is applied at some time t, then at $t+1$ the components are interchanged and the relative phase changes sign to $\delta = \pi/2$, preventing soliton formation. Similarly, if the σ_z channel is applied at t, then at $t+1$ the state $|\downarrow\rangle$ acquires a π phase, again shifting the relative phase to $\delta = \pi/2$ and destroying the soliton. Therefore, the depolarizing channel is particularly destructive to soliton stability.

[22] Dispersion can cause undesired boundary effects, so the lattice must be enlarged.



(a) (b)

Figure 15: (a) Standard deviation evolution of the noisy soliton for nine different noise levels ranging from 0.5% to 80%. (b) Instantaneous power of the standard deviation, $\alpha(t) = \frac{d\log\sigma}{d\log t}$, for the same datasets as in (a). The black dashed line indicates the diffusive regime, $\alpha = 0.5$. The color codes are identical in both subfigures, and explained in the corresponding legends.

We can also ask how these solitons will disperse in the long-time limit. To address this, we make the ansatz $\sigma \propto t^{\alpha}$, so that tracing[23] $\frac{d\log\sigma}{d\log t}$ yields the instantaneous power α, which is time-dependent, $\alpha(t)$. This is exactly what is presented in Fig. 15 (b), providing insight into the dispersion regime at time t. Here we clearly see that faster dispersion, i.e., larger $\alpha(t)$, occurs for smaller noise levels, while the opposite holds for large noise levels. However, at long times all cases tend toward the diffusive regime, which is reached more quickly for larger noise levels. Particularly enlightening is the presence of a transient regime in the small-noise curves, where little oscillations appear at early times before gradually smoothing out as the walker enters the diffusive regime.

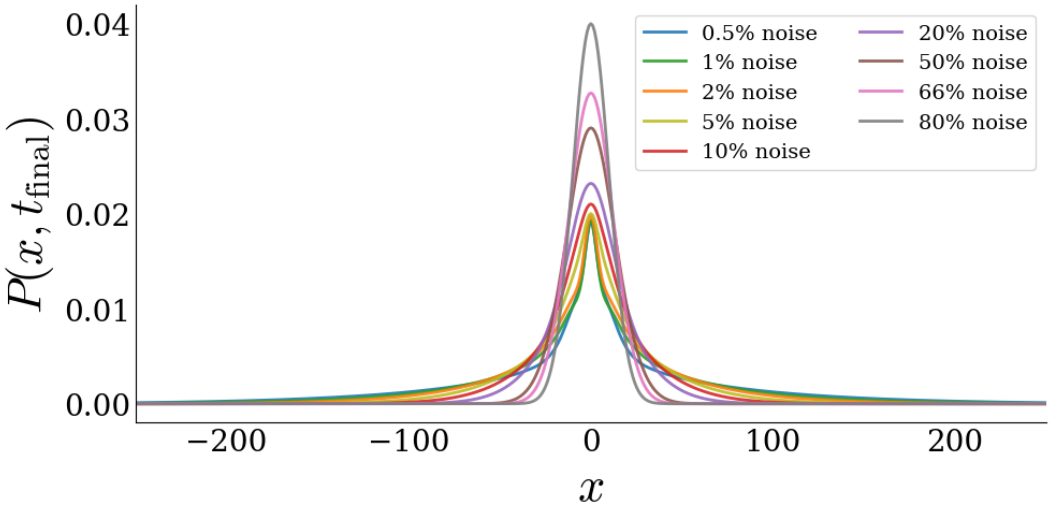


Figure 16: Final probability distribution over the lattice for the noisy solitons.

[23] log denotes the natural logarithm.

To make the walker's propagation more evident, a video comparison of the different probability space-time evolutions was prepared (see videos "Noisy NLOGB Comparison Without Noiseless" and "With Noiseless" on [27]). In this, the previously postulated behavior is confirmed. Solitons under lower noise levels appear to disperse faster, while those subject to higher noise levels transition more quickly to the dispersive regime, where they remain "stable" for longer times. This behavior is indeed reflected in Fig. 15(b) and can also be observed in Fig. 16, which shows the final evolution of the noisy solitons. Notice how higher noise levels correspond to more peaked, less-tailed curves, whereas lower noise levels produce more deformed profiles, with smaller peaks and larger tails.

In light of these results, one may also ask whether these dynamics have implications for the "quantumness" of the walker's evolution. By quantumness we refer to both the purity of the state and the coherence it possesses.

On the one hand, the purity of a quantum state is defined as

$$\text{Purity} = \text{tr}(\rho^2) \ , \tag{38}$$

with $1/d \leq \text{tr}(\rho^2) \leq 1$, where d is the dimension of the Hilbert space (2002 in our case, $2_{spin} \times 1001_x$), and 1 is the maximum value for a pure quantum state. In quantum mechanics, pure states are those that can be represented as $\rho = |\psi\rangle\langle\psi|$, whereas mixed states must be represented as convex combinations of pure states, $\rho = \sum p_i |\psi_i\rangle\langle\psi_i|$. Since purity is conserved under unitary transformations, it provides a measure of how purely quantum our state remains.

On the other hand, the coherence of a state quantifies how strongly spin-up and spin-down states are related at a given position x. Mathematically, it is encoded in the off-diagonal elements of the density matrix (see Eq. 13), whose magnitude determines the visibility of interference patterns. In our case, we analyze the global coherence, obtained by summing over lattice positions:

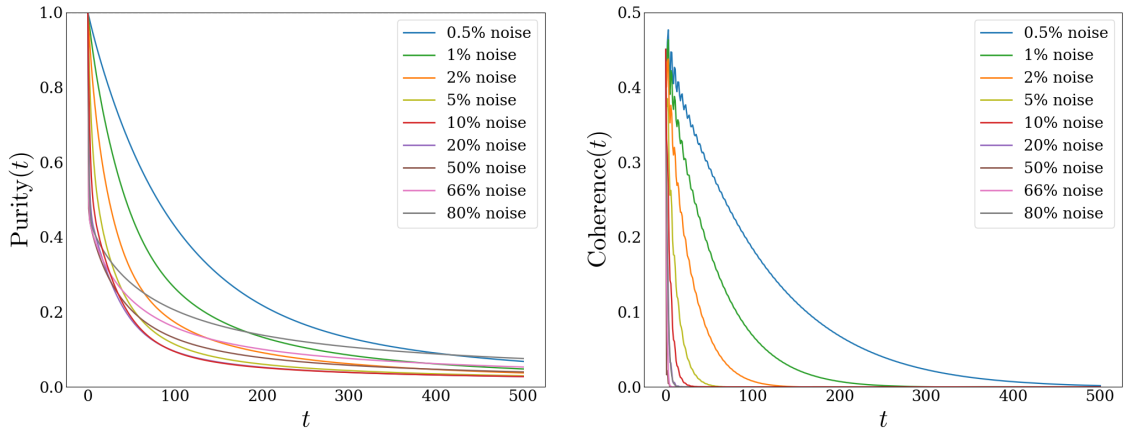
$$\langle\uparrow|\text{Tr}_x(\rho)|\downarrow\rangle = \sum_x \langle x,\uparrow|\rho|\downarrow,x\rangle = \sum_x \rho_{\uparrow\downarrow,x} \tag{39}$$

This quantity measures how well correlated the spin-up and spin-down states are across the lattice. It decreases for decoherent (classical) states and is bounded[24] as $0 \leq |\langle\uparrow|\text{Tr}_x(\rho)|\downarrow\rangle| \leq 1/2$.

In Fig. 17, we analyze precisely how the initially pure state evolves into a mixed (classical) state. Since the relation between dispersion and noise changed our perception of soliton dynamics, one might expect that solitons dispersing faster would also lose quantumness more rapidly, and vice versa. However, as shown in Fig. 17, this is not the case in our analysis, which agrees with what is generally expected ([51], Chapter 8). The higher the noise level, the stronger the decoherence: the system evolves more quickly into a fully mixed classical state, where no quantum properties are preserved.

As expected, we observe purity values ranging from 1 to nearly 0 within our time scale, and coherence values ranging from 0.5 to 0. It is also important to note that these transformations are irreversible in the sense that there is no process to recover either coherence or purity([51], Chapter 8).

[24]This bound applies to single qubit systems, but since the reduced density matrix behaves accordingly, it is also valid in our case.



(a) (b)

Figure 17: (a) Purity, $\mathrm{Tr}(\rho^2)$, as a function of time. (b) Global coherence, $\langle\uparrow|\mathrm{Tr}_x(\rho)|\downarrow\rangle$, as a function of time. The same color code as in previous plots is used.

Finally, since the long-time dispersion corresponds to that of a diffusive walk, we would expect the final probability distribution to resemble a Gaussian distribution. This would, in principle, allow us to estimate the time at which the soliton transitions into a Gaussian profile (Gaussianization). However, because the noise is applied from the very beginning of the simulation, and given that we have already observed a transient stage in which the soliton emerges (see Fig. 8), analyzing this transition directly becomes problematic. An alternative approach is to apply the noise at a later time, once the soliton is already formed. In practice, we do something similar: we save the density matrix ρ of a stable soliton (Fig. 8) at the final time, and then restrict it to the central region in order to avoid numerical fluctuations. This state can then be used to generate new solitons, with noise applied from the beginning, thereby saving computational resources (for more details see "NLOGB" and "Create solitons without transitory" in the code on [27]).

Once this is done, we need a way to characterize the soliton–Gaussian transition. To this end, we evaluate the kurtosis for the different noisy solitons. The kurtosis is defined as $k = \mu_4/\sigma^4$, where μ_4 is the fourth moment of the distribution and σ the standard deviation. It quantifies the degree of "tailedness" of the probability distribution. More commonly, one uses the excess kurtosis $k(t) - 3$, which measures the kurtosis relative to the Gaussian profile (which has $k = 3$). In our case, a distribution with excess kurtosis $k - 3 = 1.2$ corresponds to a $\mathrm{sech}^2(kx)$ profile, characteristic of a noiseless soliton. Thus, we would expect a decrease in excess kurtosis from 1.2 to 0 if a proper Gaussian profile is reached at long times.

In spite of that, as shown in Fig. 18, this only occurs in the presence of very strong noise. Although this result may appear puzzling, it is fully consistent with Fig. 16. Since kurtosis measures the relative longitude of the tails with respect to the peak, we see in Fig. 18 that smaller noise indeed leads to longer tails in the distribution and smaller peaks. The fact that the final distribution is not Gaussian is striking, because for a classical diffusive walker this is precisely what one would expect. Nevertheless, our results show that this does not necessarily occur in the noisy NLQW. See in Fig. 20, on Appendix C, how EQWs and BOs, both linear QWs, are in fact Gaussianized.

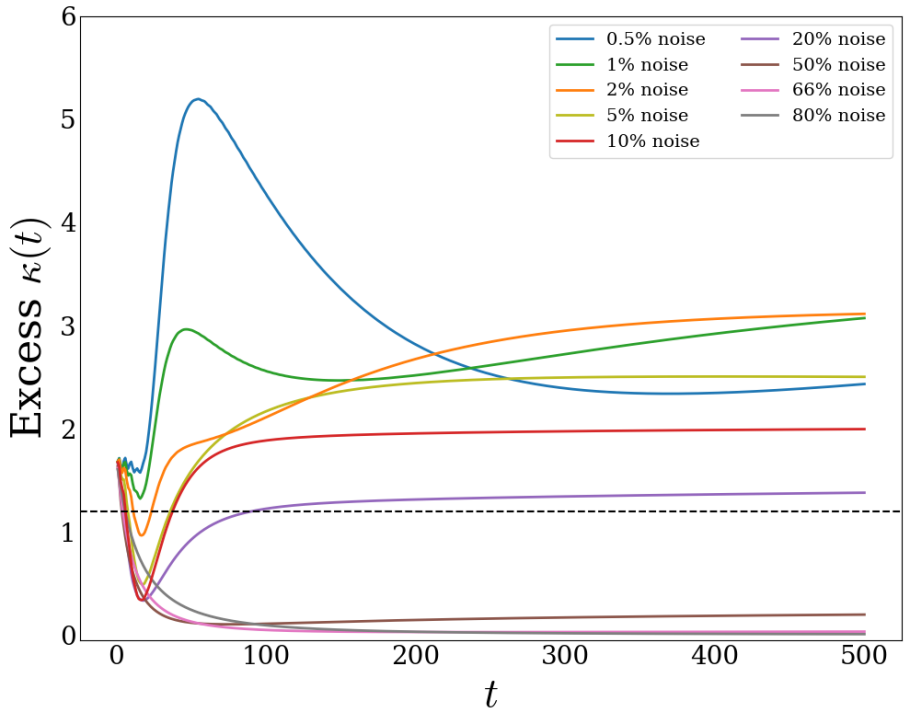


Figure 18: Evolution of the excess kurtosis for the noisy solitons, with the transient regime removed from the initial times. The black dashed line corresponds to a $\text{sech}^2(kx)$ profile.

Our conclusion is that low noisy NLQWs can sustain structures that do not vanish in the long time limit unless stronger noise is applied. This is confirmed in Appendix C: Fig. 19(a) shows that increasing the simulation time does not lead to a Gaussian distribution, while stronger noise does. Additionally, Fig. 19(b) presents a 3σ kurtosis analysis, which ensures that the overall trend is not affected by numerical fluctuations in the tails (which in principle are more sensible). So that tails and peak evolve following the same tendency.

One might also suspect that our initial soliton is not perfect, and indeed it is not. In Fig. 21(a) and (b), oscillations around the ideal values are observed both for kurtosis and for $\alpha(t)$ in the central region. These oscillations appear to be caused by numerical fluctuations during the simulation, which introduce small breathing modes in the noiseless soliton. Still, these effects are about 10^6 times smaller (in probability $P(x,t)$) than the central peak, and the 3σ analysis confirms that no significant impact should be expected from them.

5.3 The noisy NLOGB continuum limit

Since the numerical simulations revealed unexpected behavior in noisy solitons, we may ask ourselves where this originates. To address this, we perform the continuum limit of the NLOGB including the noise channels, with the aim of deriving the dynamical equations of the walker.

To perform the continuum limit of the NLOGB with noise, we first rescale the Hamiltonian in Eq. (35). Recall that when moving from discrete to continuous variables, the parameters scale

with ϵ as

$$\begin{matrix}\theta \longrightarrow \epsilon\bar{\theta} \\ \alpha \longrightarrow \epsilon\bar{\alpha}\end{matrix} \quad , \quad \text{and similarly for the probabilities} \quad \begin{matrix}\pi_x \longrightarrow \epsilon\bar{\pi}_x \\ \pi_z \longrightarrow \epsilon\bar{\pi}_z\end{matrix} \ , \tag{40}$$

so it is evident that the Hamiltonian rescales as

$$H \longrightarrow \epsilon\bar{H} \ . \tag{41}$$

With these transformations, we can now take the limit $\epsilon \to 0$ of Eq. (37). This procedure has already been well studied[25], and as shown in [28] it yields

$$\partial_t \rho(x,y,t) = -i\left[\bar{H}, \rho(x,y,t)\right] + \mathcal{L}_{\bar{\pi}}(\rho) \ , \tag{42}$$

where the Hamiltonian contribution is the rescaled version of Eq. (35), and the non-Hamiltonian (Lindblad) part is given by

$$\mathcal{L}_{\bar{\pi}}(\rho) = \bar{\pi}_x\left[\sigma_x\rho(x,y,t)\sigma_x - \rho(x,y,t)\right] + \bar{\pi}_z\left[\sigma_z\rho(x,y,t)\sigma_z - \rho(x,y,t)\right] \ . \tag{43}$$

Then, our objective is to solve the partial differential equation given in Eq. (42). In order to do this, we decompose the density matrix $\rho(x,y,t)$ in the Pauli basis as

$$\rho = \frac{1}{2} r^\mu \sigma_\mu = \frac{1}{2}\left[\mathbb{I}\, r^0 + \vec{r}\cdot\vec{\sigma}\right] \ , \tag{44}$$

where Einstein summation convention is used, and the explicit space–time dependence has been omitted for simplicity of the notation. Here, $\vec{\sigma} = (\sigma_x, \sigma_y, \sigma_z)$ is the vector of Pauli matrices, and the components $r^\mu(x,y,t) = \mathrm{Tr}_c(\rho(x,y,t)\sigma^\mu)$ represent observables acting on position space.

We then decompose the density matrix in the coin basis, where each r^μ is a Bloch vector component. The interpretation of each one is as follows: r^0 corresponds to the local probability density of the walker $\rho_{11}+\rho_{22}$, while the vector $\vec{r} = (r^1, r^2, r^3)$ encodes the spin-related degrees of freedom. In particular, r^3 measures the spin imbalance between $|\uparrow\rangle$ and $|\downarrow\rangle$, $\rho_{22}-\rho_{11}$, whereas r^1 and r^2 capture spin coherence that determine interference effects and the entanglement between spin and position. In particular, r^1 is the real part of the coherence, $\rho_{12}+\rho_{21}$, and r^2 the imaginary part, $-i(\rho_{12}-\rho_{21})$.

With this decomposition, the evolution problem becomes more tractable[26]. By substituting the expansion in Eq. (44) into Eq. (42) and performing the commutator algebra using standard Pauli matrix identities, we obtain the following system of coupled nonlinear partial differential equations

$$\begin{aligned}
\partial_t r^0 &= (\partial_x + \partial_{x'}) r^3_{xx'} \\
\partial_t r^1 &= -i(\partial_x - \partial_{x'}) r^2_{xx'} + 2\bar{\theta} r^3_{xx'} + 2\pi\bar{\alpha}\langle x|r^3 r^2|x'\rangle - 2\bar{\pi}_z r^1_{xx'} \\
\partial_t r^2 &= i(\partial_x - \partial_{x'})\partial_x r^1_{xx'} - 2\pi\bar{\alpha}\langle x|r^3 r^1|x'\rangle - 2(\bar{\pi}_z + \bar{\pi}_x) r^2_{xx'} \\
\partial_t r^3 &= (\partial_x + \partial_{x'}) r^0_{xx'} - 2\bar{\theta} r^1_{xx'} - 2\bar{\pi}_x r^1_{xx'}
\end{aligned} \ , \tag{45}$$

expressed in the position basis after applying $\langle x|$ on the left and $|x'\rangle$ on the right. Here we define $\langle x|r^\nu|x'\rangle = r^\nu_{xx'}$.

[25] See Appendix B for a review.
[26] See Appendix B for the full algebraic process.

The system of equations (45) is a coupled, nonlinear system of partial differential equations. As one can imagine, it is very difficult to solve analytically, and also challenging to solve numerically. Nevertheless, it constitutes an important result of our work and is therefore presented here. Notice that it is the same system of equations that can be found in Eqs. (51) and (52) of [28], where Arnault and colleagues take $m = -\theta$ and $2\pi_i = \gamma_i$, with the addition of the nonlinear terms. There is, however, a subtle difference between our system and that of [28]: in our case, the mass coupling term appears in r^1 instead of r^2. This small difference arises from the chosen representation, which in our case is the Weyl representation.

As a final comment, one could attempt to solve system (45) following the approach in [28], by evaluating the quantities

$$(\partial_x + \partial_{x'}) r^{\mu}_{xx'}|_{x=x'} = \partial_x R^{\mu}_x \qquad \text{and} \qquad (\partial_x - \partial_{x'}) r^{\mu}_{xx'}|_{x=-x'} = \partial_x T^{\mu}_x \ . \tag{46}$$

Still, the nonlinear terms prevent the derivation of a telegraph-like equation (see Section 4.B in [28]), since they couple r^1 and r^2 to r^3 even in the massless case. And that, maybe, could lead to the non Gaussanization of the probability distribution discussed in section 5.2.2.

Conclusions

In this thesis we have investigated the dynamics of discrete-time quantum walks (DTQWs) in the presence of external electric fields, nonlinearities, and noise, with emphasis on their behavior through numerical simulations. This constitutes a fundamental study in the context of the current NISQ devices era, where decoherence cannot be neglected.

We began by revisiting the DTQW formalism and its continuum limit, where we discussed the roles of the coin and conditional displacement operators, and introduced the density matrix formalism. With these simple but useful tools we reproduced the classical bimodal Hadamard quantum walk. Then, we reviewed the continuum limit of homogeneous quantum walks, establishing its connection with the one-dimensional Dirac equation, both under restrictions on the coin operator and in its general form.

Extending this framework, we analyzed electric quantum walks (EQWs), in which a homogeneous electric field is introduced as a position-dependent phase in the walker's coin. This model yields a wide variety of dynamical regimes. After presenting its basic building blocks, we showed its correspondence with the Dirac equation coupled to an external electric field in the continuum limit. We then explored the rich phenomenology of EQWs through numerical simulations. Distinct behaviors were identified, ranging from ballistic spreading and exact revivals [Eq. (25)] to partial revivals and Anderson localization, depending on the arithmetic properties of the field parameter. We also considered extended initial conditions, which allowed us to connect EQWs with semiclassical Bloch oscillations in solid-state physics, and finally discussed the corresponding stability conditions.

We then turned to the Nonlinear Optical Galton Board (NLOGB), a nonlinear generalization of the DTQW motivated by photonic implementations in Kerr media. After a brief historical overview, we examined its mathematical differences from linear quantum walks. We then discussed its relation to nonlinear Dirac dynamics and showed, by numerical simulations, how soliton-like wave packets emerge and persist in the noiseless case, both for extended and localized initial conditions, when the walk parameters are properly tuned.

Having introduced these models, we moved to the main contribution of this thesis: the systematic incorporation of decoherence through the depolarizing channel in numerical simulations. Our results revealed that noise profoundly alters the characteristic features of both EQWs and NLOGBs. In EQWs, revivals and localization are progressively suppressed, leading to diffusive behavior and eventual Gaussianization. In nonlinear walks, soliton stability is particularly fragile, even weak noise destroys the delicate phase relation required for soliton formation, driving the dynamics toward dispersion and loss of quantumness. We quantified these effects using measures such as standard deviation, purity, coherence, and kurtosis, and found that noise and nonlinearity interplay in a nontrivial way: soliton Gaussianization occurs only at sufficiently strong noise levels.

The noisy soliton case presented especially interesting behavior that cannot be fully understood without a continuum-limit treatment. To this end, we derived such a limit, obtaining a challenging system of equations [Eq. (45)]. Although not fully solved, this constitutes a main theoretical result of our work, opening the door to future analyses and offering connections to previous studies of diffusion in quantum walks [28].

In summary, our results highlight the fragility of quantum-walk phenomenology under realistic noisy conditions, a key limitation in the NISQ era. At the same time, the framework

developed here provides a versatile platform to study the competition between unitary evolution, nonlinearity, and decoherence. Possible directions for future work include the exploration of error-mitigation strategies, alternative noise models, and experimental implementations, with the aim of deepening our understanding of quantum walks.

Bibliography

References

[1] Zachary T. Trautt, Moneesh Upmanyu, and Alain Karma. Interface mobility from interface random walk. *Science*, 314(5799):632–635, 2006.

[2] Hamid Baghestani. Evaluating random walk forecasts of exchange rates. *Studies in Economics and Finance*, 26(3):171–181, July 2009.

[3] C. Anteneodo and W. A. M. Morgado. Critical Scaling in Standard Biased Random Walks. , 99(18):180602, November 2007.

[4] Richard B Sessions, Mark Oram, Mark D Szczelkun, and Stephen E Halford. Random walk models for dna synapsis by resolvase11edited by i. a. wilson. *Journal of Molecular Biology*, 270(3):413–425, 1997.

[5] Y. Aharonov, L. Davidovich, and N. Zagury. Quantum random walks. *Phys. Rev. A*, 48:1687–1690, Aug 1993.

[6] Andrew M. Childs. On the Relationship Between Continuous- and Discrete-Time Quantum Walk. *Communications in Mathematical Physics*, 294(2):581–603, March 2010.

[7] Andrew M. Childs, Edward Farhi, and Sam Gutmann. An Example of the Difference Between Quantum and Classical Random Walks. *Quantum Information Processing*, 1(1-2):35–43, April 2002.

[8] Oliver Mülken and Alexander Blumen. Continuous-time quantum walks: Models for coherent transport on complex networks. , 502(2-3):37–87, May 2011.

[9] Renato Portugal and Jalil Khatibi Moqadam. Efficient circuit implementations of continuous-time quantum walks for quantum search. *Entropy*, 27(5), 2025.

[10] Lov K. Grover. A fast quantum mechanical algorithm for database search. *arXiv e-prints*, pages quant–ph/9605043, May 1996.

[11] Ugo Nzongani, Julien Zylberman, Carlo-Elia Doncecchi, Armando Pérez, Fabrice Debbasch, and Pablo Arnault. Quantum circuits for discrete-time quantum walks with position-dependent coin operator. *Quantum Information Processing*, 22(7):270, July 2023.

[12] Rei Sato and Kazuhiro Saito. Circuit Implementation of Discrete-Time Quantum Walks on Complex Networks. *arXiv e-prints*, page arXiv:2408.15653, August 2024.

[13] W. Dür, Robert Raussendorf, V. Kendon, and H. Briegel. Quantum walks in optical lattices. *Physical Review A*, 66, 07 2002.

[14] Ben Travaglione. Implementing the quantum random walk. *Phys. Rev. A*, 65, 02 2002.

[15] H. Schmitz, R. Matjeschk, Ch. Schneider, J. Glueckert, M. Enderlein, T. Huber, and T. Schaetz. Quantum walk of a trapped ion in phase space. *Phys. Rev. Lett.*, 103:090504, Aug 2009.

[16] Xiang Zhan, Lei Xiao, Zhihao Bian, Kunkun Wang, Xingze Qiu, Barry C. Sanders, Wei Yi, and Peng Xue. Detecting topological invariants in nonunitary discrete-time quantum walks. *Phys. Rev. Lett.*, 119:130501, Sep 2017.

[17] M. S. Rudner and L. S. Levitov. Topological transition in a non-hermitian quantum walk. *Phys. Rev. Lett.*, 102:065703, Feb 2009.

[18] Himanshu Sahu and C. M. Chandrashekar. Open system approach to neutrino oscillations in a quantum walk framework. *Quantum Information Processing*, 23(1):7, January 2024.

[19] Giuseppe Di Molfetta, Marc Brachet, and Fabrice Debbasch. Quantum walks in artificial electric and gravitational fields. *Physica A Statistical Mechanics and its Applications*, 397:157–168, March 2014.

[20] C. Cedzich, T. Geib, A. H. Werner, and R. F. Werner. Quantum walks in external gauge fields. *Journal of Mathematical Physics*, 60(1):012107, January 2019.

[21] Andreu Anglés-Castillo and Armando Pérez. A quantum walk simulation of extra dimensions with warped geometry. *Scientific Reports*, 12:1926, February 2022.

[22] John Preskill. Quantum Computing in the NISQ era and beyond. *Quantum*, 2:79, August 2018.

[23] Anandu Kalleri Madhu, Alexey A. Melnikov, Leonid E. Fedichkin, Alexander P. Alodjants, and Ray-Kuang Lee. Quantum walk processes in quantum devices. *Heliyon*, 9(3):e13416, March 2023.

[24] Andrea Mammola, Quentin Schaeverbeke, and Giuseppe Di Molfetta. Noisy simulations of Quantum Walk and Quantum Walk search via Quantum Cellular Automata on a semiconducting spin processor emulator. *arXiv e-prints*, page arXiv:2505.14134, May 2025.

[25] Pablo Arnault. Discrete-time quantum walks and gauge theories. *arXiv e-prints*, page arXiv:1710.11123, October 2017.

[26] Andris Ambainis, Eric Bach, Ashwin Nayak, Ashvin Vishwanath, and John Watrous. One-dimensional quantum walks. *Conference Proceedings of the Annual ACM Symposium on Theory of Computing*, 12 2001.

[27] Andreu Benavent Montell. Python code for the obtantion of the quantum walks data and relevant video comparisons. https://github.com/AndreuBM/Master-Thesis-noisy-NLQWs.

[28] Pablo Arnault, Adrian Macquet, Andreu Anglés-Castillo, Iván Márquez-Martín, Vicente Pina-Canelles, Armando Pérez, Giuseppe Di Molfetta, Pablo Arrighi, and Fabrice Debbasch. Quantum simulation of quantum relativistic diffusion via quantum walks. *Journal of Physics A Mathematical General*, 53(20):205303, May 2020.

[29] Maximilian Genske, Wolfgang Alt, Andreas Steffen, Albert H. Werner, Reinhard F. Werner, Dieter Meschede, and Andrea Alberti. Electric Quantum Walks with Individual Atoms. , 110(19):190601, May 2013.

[30] C. Cedzich, T. Rybár, A. H. Werner, A. Alberti, M. Genske, and R. F. Werner. Propagation of Quantum Walks in Electric Fields. , 111(16):160601, October 2013.

[31] T Hartmann, F Keck, H. Korsch, and S Mossmann. Dynamics of bloch oscillations. *New Journal of Physics*, 6, 01 2004.

[32] F Domínguez-Adame. Beyond the semiclassical description of bloch oscillations. *European Journal of Physics*, 31(3):639, apr 2010.

[33] C. Cedzich and A. H. Werner. Anderson Localization for Electric Quantum Walks and Skew-Shift CMV Matrices. *Communications in Mathematical Physics*, 387(3):1257–1279, November 2021.

[34] Pablo Arnault and Fabrice Debbasch. Quantum walks and discrete gauge theories. *Phys. Rev. A*, 93:052301, May 2016.

[35] Pablo Arnault, Benjamin Pepper, and A. Pérez. Quantum walks in weak electric fields and bloch oscillations. *Phys. Rev. A*, 101:062324, Jun 2020.

[36] D. Bouwmeester, I. Marzoli, G. P. Karman, W. Schleich, and J. P. Woerdman. Optical galton board. *Phys. Rev. A*, 61:013410, Dec 1999.

[37] Barry C. Sanders, Stephen D. Bartlett, Ben Tregenna, and Peter L. Knight. Quantum quincunx in cavity quantum electrodynamics. *Phys. Rev. A*, 67:042305, Apr 2003.

[38] Eugenio Roldán and J. Soriano. Optical implementability of the two-dimensional quantum walk. *Journal of Modern Optics*, 52, 03 2005.

[39] C. Navarrete-Benlloch, A. Pérez, and Eugenio Roldán. Nonlinear optical galton board. *Phys. Rev. A*, 75:062333, Jun 2007.

[40] P. G. Drazin and R. S. Johnson. *Solitons: An Introduction*. Cambridge Texts in Applied Mathematics. Cambridge University Press, 2 edition, 1989.

[41] Martin Wimmer, Alois Regensburger, Christoph Bersch, Mohammad-Ali Miri, Sascha Batz, Georgy Onishchukov, Demetrios Christodoulides, and Ulf Peschel. Optical diametric drive acceleration via action-reaction symmetry breaking. *Nat. Phys.*, 9, 10 2013.

[42] Giuseppe Di Molfetta, F. Debbasch, and Marc-Etienne Brachet. Nonlinear optical galton board: thermalization and continuous limit. *Physical Review E*, 92, 06 2015.

[43] Chang-Woo Lee, Paweł Kurzyński, and Hyunchul Nha. Quantum walk as a simulator of nonlinear dynamics: Nonlinear dirac equation and solitons. *Physical Review A*, 92, 11 2015.

[44] Pedro Nicácio Falcão, João Mendonça, Anderson Buarque, Wandearley Dias, G. Almeida, and Marcelo Lyra. Nonlinear three-state quantum walks. *Physical Review A*, 106, 07 2022.

[45] Frederico Passos and Anderson Buarque. Nonlinear flip-flop quantum walks through potential barriers. *Physical Review A*, 106, 12 2022.

[46] Andreu Anglés-Castillo, Armando Pérez, and Eugenio Roldán. Solitons in a photonic nonlinear quantum walk: lessons from the continuum. *arXiv e-prints*, page arXiv:2308.01014, August 2023.

[47] Jianke Yang. Stable Embedded Solitons. , 91(14):143903, October 2003.

[48] P. Cappellaro,. Lecture notes for 22.51 quantum theory of radiation interactions, fall 2012. https://opencw.aprende.org/courses/nuclear-engineering/22-51-quantum-theory-of-radiation-interactions-fall-2012/lecture-notes/, 2012. Chapter 8: Open Quantum Systems.

[49] J. Preskill. Quantum information and computation (caltech), 2012. Chapter 3.4 : Three Quantum Channels,.

[50] Andrei Polyanin. *Handbook of Linear Partial Differential Equations for Engineers and Scientists*. 01 2002.

[51] Michael A. Nielsen and Isaac L. Chuang. *Quantum Computation and Quantum Information: 10th Anniversary Edition*. Cambridge University Press, 2010.

[52] G. H. Hardy and E. M. Wright. *An Introduction to the Theory of Numbers*. Oxford, fourth edition, 1975.

[53] Daniel Manzano. A short introduction to the Lindblad master equation. *AIP Advances*, 10(2):025106, February 2020.

Appendix A: Continued fraction expansion

A continued fraction expansion [52] is an expression of the form

$$x = c_0 + \cfrac{1}{c_1 + \cfrac{1}{c_2 + \cfrac{1}{c_3 + \cfrac{1}{c_4 + \cdots}}}} , \tag{47}$$

where $c_0 = \lfloor x \rfloor$ and $c_i \in \mathbb{N}$[27] for $i \geq 0$, given $x \in \mathbb{R}^+$. We can then write compactly $x = [c_0, c_1, c_2, c_3, \ldots]$.

Notice this fraction can be truncated at some $i \leq N$ so that the number x is well approximated by

$$\frac{n_i}{m_i} = [c_0, c_1, \ldots, c_i] \tag{48}$$

where the integers n_i and m_i are defined recursively as

$$\begin{array}{llll} n_0 = c_0 \ , & n_1 = c_1 c_0 + 1 & n_i = c_i n_{i-1} + n_{i-2} & (2 \leq i \leq N) \\ m_0 = 1 \ , & m_1 = c_0 & m_i = c_i m_{i-1} + m_{i-2} & (2 \leq i \leq N) \end{array} \ . \tag{49}$$

From this rational approximation to x, one can also prove that

$$\left| x - \frac{n_i}{m_i} \right| \leq \frac{1}{c_{i+1} m_i^2} \ . \tag{50}$$

At first glance, this inequality shows that large c_i terms correspond to good approximations. For example, the number $\pi = [3, 7, 15, \ldots]$ has a rational approximation to second order, $\pi \approx 22/7$, with error $< 1/(15 \cdot 49) \approx 10^{-3}$. In this sense, the most "irrational" numbers are the golden ratio $\varphi = (\sqrt{5}+1)/2 = [1, 1, 1, 1, \ldots]$[28], followed by the silver ratio $\sigma = 1 + \sqrt{2} = [2, 2, 2, 2, 2, \ldots]$, which can never be well approximated by rationals.

[27] c_0 may be negative in some cases.

[28] Same for its reciprocal used throughout the thesis.

Appendix B: Lindblad Eq. and PDEs for the NLOGB

In this Appendix, we derive Eq. (42) starting from Eq. (37). To do so, we use the rescaled Hamiltonian introduced in Eq. (41), so that Eq. (37) can be rewritten as

$$\rho(x,t+\epsilon) = (1-\epsilon(\bar{\pi}_x+\bar{\pi}_z))\, e^{-i\epsilon\bar{H}}\rho(x,t)e^{i\epsilon\bar{H}} + \epsilon\bar{\pi}_x\,\sigma_x\rho(x,t)\sigma_x + \epsilon\bar{\pi}_z\,\sigma_z\rho(x,t)\sigma_z\ . \tag{51}$$

We now expand the exponentials to first order in ϵ and discard terms of order $\mathcal{O}(\epsilon^2)$. This yields

$$\begin{aligned}\rho(x,t+\epsilon) =&\rho(x,t) + i\epsilon\left[\rho(x,t)\bar{H} - \bar{H}\rho(x,t)\right] - \\ &-\epsilon(\bar{\pi}_x+\bar{\pi}_z)\rho(x,t) + \epsilon\left[\bar{\pi}_x\,\sigma_x\rho(x,t)\sigma_x + \bar{\pi}_z\,\sigma_z\rho(x,t)\sigma_z\right]\ ,\end{aligned} \tag{52}$$

which, upon recognizing the commutator $\left[\bar{H},\rho(x,t)\right]$ and regrouping terms, leads to

$$\begin{aligned}&\lim_{\epsilon\to 0}\left(\frac{\rho(x,t+\epsilon)-\rho(x,t)}{\epsilon}\right) = \partial_t\rho(x,t) = \\ &-i\left[\bar{H},\rho(x,t)\right] + \bar{\pi}_x\left[\sigma_x\rho(x,t)\sigma_x - \rho(x,t)\right] + \bar{\pi}_z\left[\sigma_z\rho(x,t)\sigma_z - \rho(x,t)\right]\ ,\end{aligned} \tag{53}$$

which is precisely Eq. (42). This equation is in the form of the so-called Lindblad master equation [53]

$$\partial_t\rho = -i[H,\rho] + \sum_k \gamma_k\left(L_k\rho L_k^\dagger - \frac{1}{2}\left\{L_k^\dagger L_k,\rho\right\}\right), \tag{54}$$

where $k=1,2$, with $L_1=\sigma_x$ and $L_2=\sigma_z$ the Lindblad (jump) operators. These act on the Hilbert space of the system and, in general, may be non-Hermitian (though they are in our case). The coefficients γ_k are non-negative real numbers that determine the "strength" of each dissipative channel.

Another important step is the derivation of the system of Eqs. (45). To obtain it, we start from Eq. (42) and introduce the Pauli decomposition given in Eq. (44). First, we rewrite the Hamiltonian as

$$\bar{H} = \bar{\theta}\sigma_y - i\partial_x\sigma_z - \pi\bar{\alpha}\left[r^0\mathbb{I} + r^3\sigma_z\right]\ , \tag{55}$$

where we have expressed the nonlinear term using the definition of the projectors in Eq. (30), together with

$$\begin{aligned}\rho_{11}(x,t) &= \langle\uparrow|\rho(x,t)|\uparrow\rangle = \frac{1}{2}\left[r^0\mathbb{I} + r^3\sigma_z\right]\ ,\\ \rho_{22}(x,t) &= \langle\downarrow|\rho(x,t)|\downarrow\rangle = \frac{1}{2}\left[r^0\mathbb{I} - r^3\sigma_z\right]\ .\end{aligned} \tag{56}$$

Now, the commutator in Eq. (42) becomes more straightforward to evaluate. To expand the equation, we use the Pauli matrix identities

$$[\sigma_i,\sigma_j] = 2i\,\epsilon_{ijk}\sigma_k\ , \qquad \text{and} \qquad \sigma_i\sigma_j\sigma_i = -\sigma_j \quad \text{for } i\neq j\ . \tag{57}$$

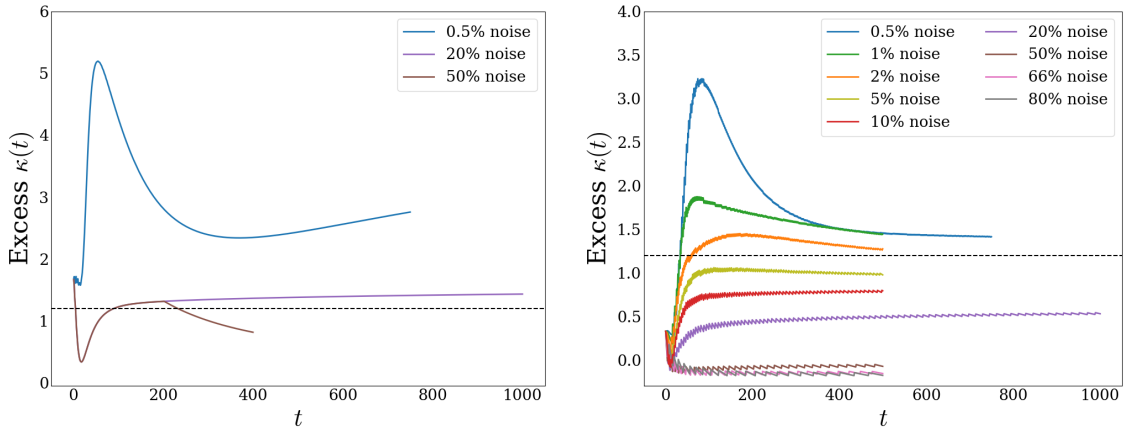
Applying these identities and rearranging terms, we obtain

$$\begin{aligned}\partial_t\rho(x,t) = &\left(-\frac{i}{2}[\hat{p},r^3]\right)\mathbb{I}_c \\ &+\left(\bar{\theta}r^3-\frac{1}{2}\{\hat{p},r^2\}+\pi\bar{\alpha}r^3r^2-\bar{\pi}_z r^1\right)\sigma_x \\ &+\left(\frac{1}{2}\{\hat{p},r^1\}+\pi\bar{\alpha}r^3r^1-(\bar{\pi}_x+\bar{\pi}_z)r^2\right)\sigma_y \\ &+\left(-i\frac{1}{2}[\hat{p},r^0]-\bar{\pi}_x r^3-\bar{\theta}r^1\right)\sigma_z\ ,\end{aligned} \tag{58}$$

where $[A,B]=AB-BA$ and $\{A,B\}=AB+BA$ are respectively the commutator and anti-commutator operations. To obtain the system of equations (45), we project onto the coin basis by taking the partial trace $\mathrm{Tr}(\sigma_i\,\partial_t\rho)=\partial_t r^i$ and then move to the position basis by multiplying $\langle x|$ on the left and $|x'\rangle$ on the right. Using the orthogonality relation $\mathrm{Tr}(\sigma_i\sigma_j)=2\delta_{ij}$ and $\hat{p}|x\rangle=-i\partial_x|x\rangle$, we arrive at the system of Eqs. (45).

Appendix C: Additional material

In this Appendix, we present additional analyses for the noisy soliton case in order to further justify our results.



(a) (b)

Figure 19: (a) Kurtosis excess for three different simulations with modified parameters. The blue curve corresponds to a NLQW on a lattice $x \in [-750, 750]$ stopped at $t = 750$. The brown curve corresponds to a lattice $x \in [-300, 300]$, where at $t = 200$ the noise level is increased from 20% to 50%. The purple curve corresponds to a lattice $x \in [-400, 400]$ stopped at $t = 1000$. (b) 3σ kurtosis analysis around the center of the noisy soliton. The overall trend is similar to that of the full system, see Fig. 18. For this analysis, the longer-time simulations from (a) were included.

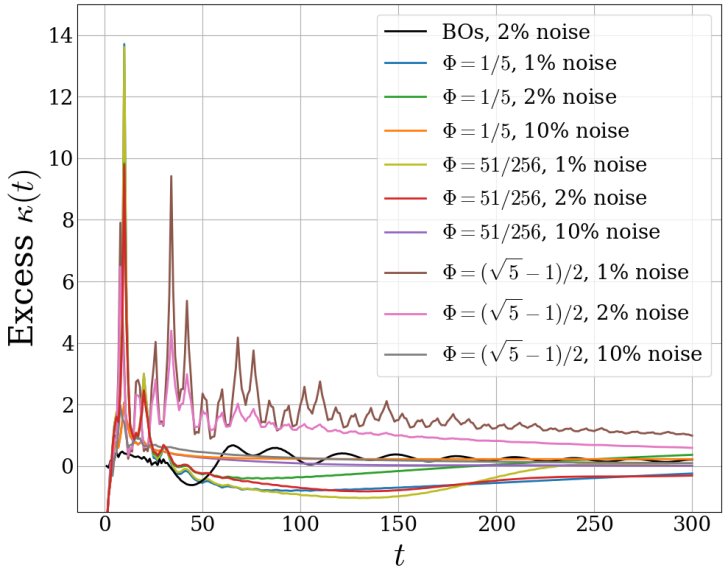
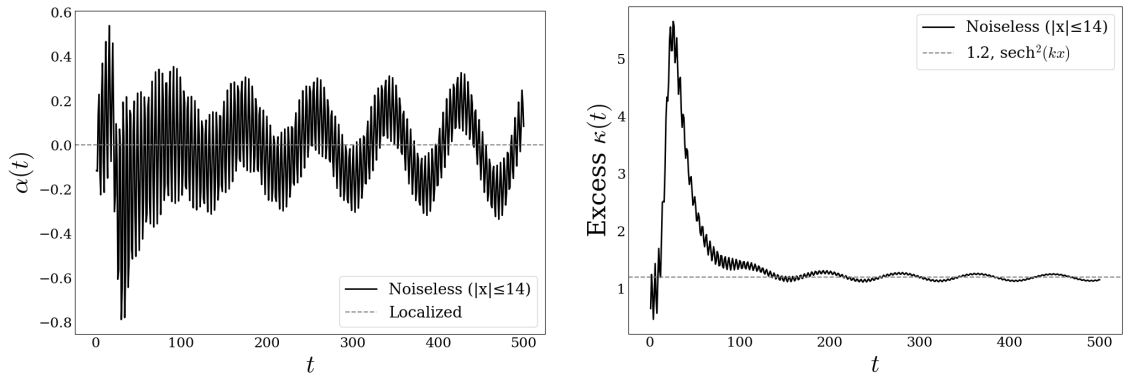


Figure 20: Evolution of the excess kurtosis for the noisy EQWs and BOs presented throughout the thesis.



(a) (b)

Figure 21: (a) Instantaneous power of the standard deviation, $\alpha(t) = \frac{d \log \sigma}{d \log t}$, for the central region of a noiseless soliton. (b) Kurtosis excess for the central region of the same noiseless soliton.